工學碩士 學位論文

The electrical properties of Schottky diodes based on $Mg_xZn_{1-x}O$ thin films deposited by RF magnetron co-sputtering

指導敎授 金 泓 承

2016年 2月

韓國海洋大學校 大學院

電子材料工學科

嶽 麗 麗

本 論文을 嶽麗麗의

工學碩士 學位論文으로 認准함.

委員長　　　梁　　瑠　　（印）

委　員　　　金　泓　承　（印）

委　員　　　張　樂　元　（印）

2016年 2月

韓國海洋大學校 大學院

Contents

List of Tables

List of Figures

The electrical properties of Schottky diodes based on $Mg_xZn_{1-x}O$ thin films deposited by RF magnetron co-sputtering

Lili Yue

Department of Electronic Material Engineering
Graduate School of Korea Maritime and Ocean University

Abstract

Optoelectronic devices operating in ultraviolet region have attracted much attention in recent years for their potential applications in flame sensing, chemical/biological agents detection, convert communications, missile plume sensing, air and water purification, etc.. Ternary $Mg_xZn_{1-x}O$ alloy material, with a tunable band gap in the range of 3.37-7.8 eV, is a promising candidate for optoelectronic devices that covers a broad portion of DUV spectrum. Moreover, compared with other wide band gap semiconductors, $Mg_xZn_{1-x}O$ has various unique features, such as the high resistance to radiation, the amenability to conventional wet chemistry etching, the environmentally friendly characters, and the relatively low growth temperatures. Many methods have been proposed to prepare $Mg_xZn_{1-x}O$ films, such as chemical vapor deposition, electro-deposition, spray pyrolysis, pulsed laser deposition, the sol-gel method technique, and radio frequency (RF) magnetron sputtering. Among these methods, RF magnetron sputtering is preferred due to its low cost, simplicity, and low process temperature. But up to now, good-quality wurtzite $Mg_xZn_{1-x}O$ films with high Mg content deposited by RF magnetron co-sputtering are rare. So we used RF

magnetron co-sputtering with ZnO and $Mg_{0.3}Zn_{0.7}O$ targets to deposit wurtzite $Mg_xZn_{1-x}O$ films on Si substrate. The Mg content could be varied from 0 at.% to 30 at.% by controlling the RF power of $Mg_{0.3}Zn_{0.7}O$ target.

Chapter 1 is the introduction of this study. In chapter 2, the basic properties of ZnO, MgO, and $Mg_xZn_{1-x}O$, the application of $Mg_xZn_{1-x}O$, the concept of Metal-Semiconductor contact, and the *I-V* characteristics of Schottky diode were introduced. In chapter 3, the experiment and analysis methods were described. The structural and electrical properties of $Mg_xZn_{1-x}O$ ($0 \leq x \leq 0.18$) thin films as the function of Mg content were investigated in chapter 4. The Schottky contact properties of $Mg_xZn_{1-x}O$ thin films with Ag metal as the function of Mg content were studied in chapter 4. The effect of metal materials on Schottky contact properties of $Mg_{0.18}Zn_{0.82}O$ thin film were also investigated in chapter 4. In the final chapter, the results were summarized and concluded.

KEY WORDS: $Mg_xZn_{1-x}O$; Thin films; Structural properties; Electrical properties; Schottky diode; RF magnetron co-sputtering;
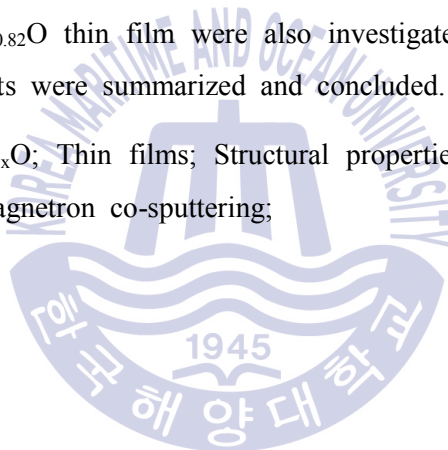
Chapter 1. Introduction

ZnO has emerged as an exciting new material in solid state electronics field owing to (1) its large exciton binding energy (60 meV) that inhibits thermal activation and enhances light emission at room temperature [1], (2) its radiation hardness [2, 3], (3) the ease with which it forms nanostructures that can emit light and sense charge transfer efficiently, (4) the abundance of Zn compared with the limited availability of Ga and In, (5) its etch ability with wet chemicals [4], and (6) its biocompatibility [5]. As a member of ZnO material family, ternary $Mg_xZn_{1-x}O$ material, with a tunable band gap from 3.37 eV to 7.8 eV, has received much attention due to their potential applications in short-wavelength optoelectronic devices, such as flame sensing, chemical/biological agents detection, convert communications, missile plume sensing, air and water purification [6].

However, there is large crystal structure dissimilarity between wurtzite-hexagonal ZnO and rock-salt-cubic MgO, which leads to unstable phase mixing [7]. In the phase diagram of the ZnO-MgO binary system, the thermodynamic solubility limit of MgO in ZnO is only 4 at.% [8]. $Mg_xZn_{1-x}O$ films grown via pulsed laser deposition (PLD) were found to exceed the low solubility limit of MgO in ZnO due to the thermodynamic growth conditions, and single phase films with the wurtzite structure of up to 33 at.% Mg were achieved [9]. Other deposition techniques also have been proposed to prepare $Mg_xZn_{1-x}O$ film, such as chemical vapor deposition, electro-deposition, spray pyrolysis, the sol-gel method technique, and radio frequency (RF) magnetron sputtering. Among these methods, RF magnetron sputtering is preferred due to its low cost, simplicity, and low process temperature. Compared with the sputtering method with single MgZnO target with a fixed Mg composition, co-sputtering has a superior advantage. That is, the $Mg_xZn_{1-x}O$ films with various Mg contents can be deposited only with two targets and the Mg contents can be varied by controlling the power or the area of target. J. P. Kar et al. [10] have grown the $Mg_xZn_{1-x}O$ (x=0.03) nanowire on ZnO buffer layer by co-sputtering ZnO and Mg targets. Y. Y Kim et al. [11] have fabricated

the $Mg_xZn_{1-x}O/ZnO$ (x=0.8, 0.16) heterojunction by co-sputtering ZnO and MgO targets. However, without buffer layer, Kang et al. [12] have deposited the $Mg_xZn_{1-x}O$ film on Si (001) substrate by co-sputtering with ZnO and MgO targets and the maximum Mg content was only 7 at.%, even though used the relatively high power of MgO target. Because the MgO target has very low sputtering yield, the MgO target is difficult to sputter. Therefore, the good-quality wurtzite $Mg_xZn_{1-x}O$ films with high Mg content are rare. A. Ohtomo et al. [9] reported that the wurtzite $Mg_xZn_{1-x}O$ films deposited by PLD can be maintained to 33 at.%, so we expect to co-sputter the $Mg_{0.3}Zn_{0.7}O$ and ZnO targets to deposit the wurtzite $Mg_xZn_{1-x}O$ films with the Mg content range from 0 at.% to 30 at.%. Moreover, the $Mg_{0.3}Zn_{0.7}O$ target has higher sputtering yield than MgO target, it is feasible to increase the incorporation ratio of Mg into ZnO. So by co-sputtering ZnO and $Mg_{0.3}Zn_{0.7}O$ targets, the Mg content could be varied from 0 at.% to 30 at.% by varying the RF power of $Mg_{0.3}Zn_{0.7}O$ target.

This dissertation investigates the structural and electrical properties of $Mg_xZn_{1-x}O$ thin films which were deposited by RF magnetron co-sputtering with ZnO and $Mg_{0.3}Zn_{0.7}O$ targets on Si substrate. The Mg content was varied from 0 at.% to 18 at.% by controlling the power of $Mg_{0.3}Zn_{0.7}O$ target. And the effect of Mg content and metal materials on the Schottky contact properties of $Mg_xZn_{1-x}O$ thin films were studied. The first chapter is the introduction of this study. Chapter 2 introduces the review of literature which includes the general properties of ZnO, MgO, and MgZnO, the application of MgZnO, the concept of Metal-Semiconductor contact, and the *I-V* characteristics of Schottky diode. The third chapter describes the experiment and analysis methods. Chapter 4 investigates the structural and electrical properties of $Mg_xZn_{1-x}O$ ($0 \le x \le 0.18$) thin films as the function of Mg content. The Schottky contact properties of $Mg_xZn_{1-x}O$ thin films as the function of Mg concentration with Ag metal were studied in chapter 4. The effect of metal materials on Schottky contact properties of $Mg_{0.18}Zn_{0.82}O$ thin film is also reported here. The final chapter contains the conclusion and summary of this dissertation.

Chapter 2. Literature survey

2.1 Physical properties of ZnO

ZnO materials are II-VI compound semiconductor whose ionicity resides at the borderline between covalent and ionic semiconductor [13]. The crystal structure of ZnO includes zinc blende (B3), wurtzite (B4), and rocksalt (B1), as schematically shown in Figure 2.1 [14]. The wurtzite ZnO structure which is composed of two interpenetrating hexagonal-close-packed (hcp) sublattices is the thermodynamically stable phase at ambient conditions. The hexagonal crystal structure with a=3.24 Å and c=5.12 Å belongs to the space group of P63mc. The Zn atoms in hexagonal wurtzite structure are tetrahedrally coordinated to four O atoms, or vice versa, where Zn s electrons hybridize with O p electrons [13]. And along the [0001] direction in Figure 2.1 (b) the Zn cation and O anion connected by dashed lines attracted to each other by electrostatic force. That is why the hexagonal wurtzite ZnO resides at the borderline between covalent and ionic semiconductor.
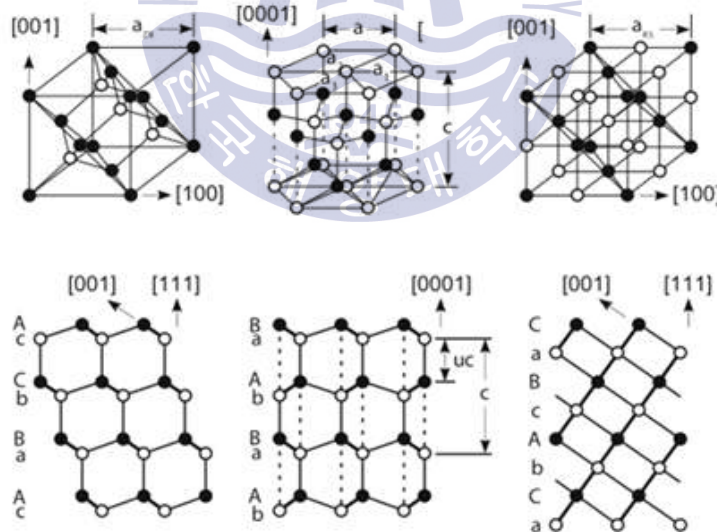
(a) Zinc blende (B3)   (b) Wurtzite (B4)   (c) Rocksalt (B1)

Fig. 2.1 The crystal structure of (a) cubic zinc blende, (b) hexagonal wurtzite, and (c) cubic rock salt structure, closed and open circle represent cation and anion [14]

- 3 -

ZnO is a wind bandgap and direct band compound semiconductor. The valence band (VB) of pure ZnO is formed by the Zn-3d states and the O-2p states, and the conduction band (CB) is mainly formed by the 4s states of Zn and the 2s states of O. Moreover, the conduction band minimum (CBM) and the valence band maximum (VBM) are formed by Zn-4s states and the O-2p states [15]. The band gap width of ZnO is 3.37 eV and can be tuned via divalent substitution on the cation site. For example, the replacement of Zn by Mg increases the band gap of ZnO from 3.37 eV to 7.8 eV and Cd substitution caused a reduction in the band gap to ~3.0 eV [16].

Table 2.1 [17] shows the physical properties of ZnO. These properties make it to be an exciting new material in solid state electronics field.

Table 2.1 Properties of ZnO material [17]

Properties	Value
Lattice parameter at 300K a_0 c_0 c_0/a_0	0.32495 nm 0.52069 nm 1.602 (ideal value = 1.6333)
u	0.345
Density	5.606 g/cm^3
Stable phase at 300K	Wurtzite
Melting temperature	1975 ^{o}C
Linear expansion coefficient (/^{o}C)	a_0: 6.5 x 10^{-6} c_0: 3.0 x 10^{-6}
Static dielectric constant	8.656
Refractive index	2.008, 2.029
Energy band gap	3.4 eV, direct
Intrinsic carrier concentration	<10^6 cm^{-3}
Exciton binding energy	60 meV
Electron effective mass	0.24
Electron Hall mobility at 300K for n-type conductivity	200 cm^2/Vs
Hole effective mass	0.59
Hole Hall mobility at 300K for low p-type conductivity	5-50 cm^2/Vs

2.2 Physical properties of MgO

Magnesium oxide (MgO), with a wind band gap of 7.8 eV, is a II-VI binary compound metal semiconductor. MgO generally form in rock salt structure (as shown in Figure 2.1 c) with lattice constant a = 4.21 Å. The structure of MgO consists of two interpenetrating fcc lattices of oxygen anions and metal cations in +2 oxidation state, making these oxides even more ionic than prototypical ionic NaCl.

MgO is an interesting material being transparent, thermally stable, and having high electrical resistivity [18] and has attracted considerable interest as a material for a broad spectrum of electronic applications ranging from gate insulators in metal-oxide-semiconductor (MOS) transistors to a buffer layer enabling integration of other functional oxides [19]. Moreover, MgO can be alloyed with ZnO to control the band gap of ZnO system. The properties of MgO are summarized in Table 2.2.

Table 2.2 Properties of MgO material [17]

Properties	Value
Lattice constant	a = 0.4216 nm
Crystal structure at 300K	cubic rock salt
Band gap energy	7.8 eV
Density	3.576 g/cm^3
Melting point	2.852 ^{o}C
Boiling point	3,600 ^{o}C
Thermal conductivity at 300K	45-60 W·m^{-1}·K^{-1}
Refractive index	1.736
Dielectric constant	9.83
Linear expansion coefficient (/^{o}C)	10.5 x 10^{-6}

2.3 Physical properties of $Mg_xZn_{1-x}O$

2.3.1 Structural properties of $Mg_xZn_{1-x}O$

Ternary $Mg_xZn_{1-x}O$ alloy is a ZnO and MgO solid solution material. Since the ionic radius of Mg^{2+} (0.57 Å) is close to that of Zn^{2+} (0.6 Å), the replacement of Zn by Mg should not cause a significant change of the lattice constant. However, a large crystal structure dissimilarity between the wurtzite-hexagonal ZnO and the rock-salt-cubic MgO can cause unstable phase mixing [7]. Depending on growth conditions, $Mg_xZn_{1-x}O$ may have a hexagonal or cubic lattice (Figure 2.2).
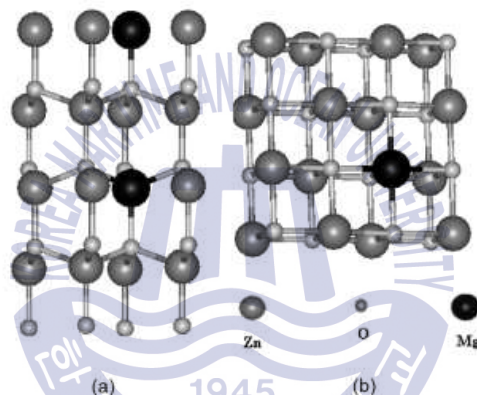
Fig. 2.2 The structural models of hexagonal (a) and cubic (b) MgZnO alloys [7]

Despite the similarity between the Zn^{2+} and Mg^{2+} ionic radii, the thermodynamic solubility limit of MgO in ZnO is less than 4 at.% [8]. In 1998, Ohtomo et al.[9] have fabricated $Mg_xZn_{1-x}O$ films by PLD and the hexagonal structure was maintained to 33 at.%, which presented the possibility of growing wurtzite $Mg_xZn_{1-x}O$ films with high Mg content. So it is possible to produce $Mg_xZn_{1-x}O$ with a higher Mg percentage by using a non-equilibrium thermodynamic growth condition, however, a phase separation of the lattice can occur. In this condition, $Mg_xZn_{1-x}O$ structure is made from hexagonal and cubic microcrystals simultaneously. In 2003, Takeuchi et al. [20] have fabricated $Mg_xZn_{1-x}O$ films by

PLD at substrate temperature of 600 ℃ and found the phase separation region of the phase diagram in the range of $0.37 \leq x \leq 0.6$. However, L. K. Wanga et al. [21] have growth the cubic $Mg_xZn_{1-x}O$ layer with $x=0.33$ by using MOCVD technique. The stability of material depends on the difference between the total energies of cubic and hexagonal lattice structures, and also depends on temperature because the total energy of different lattice structures changes at different rates with the changing temperature [22]. Since $Mg_xZn_{1-x}O$ has the most unstable structure with x values around 0.5, usually it grows with a mixed phase lattice structure at these x values. The composition tuned $Mg_xZn_{1-x}O$ band gap and the corresponding phases is shown in Figure 2.3. The shaded area is the phase separated region $(0.37 \leq x \leq 0.6)$ that has no well defined band gap [20].
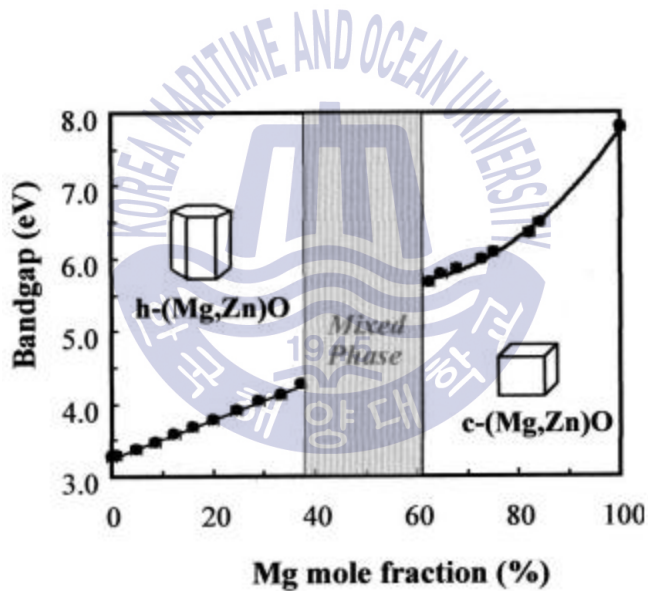
Fig. 2.3 Composition tuned $Mg_xZn_{1-x}O$ band gap and the corresponding phases [24]

2.3.2 Optical-electrical properties of $Mg_xZn_{1-x}O$

ZnO and MgO have bandgap energies of 3.37 eV and 7.8 eV, respectively. The bandgap of $Mg_xZn_{1-x}O$ can be tuned from 3.37 eV to 7.8 eV by controlling the Mg content. It has been observed that exciton binding energy in $Mg_xZn_{1-x}O$ has approximately the same value like in ZnO (60 meV at RT.) [23]. Absorption spectra for $Mg_xZn_{1-x}O$ at room temperature are shown in Figure 2.4. Clearly expressed peak reveals that the excitonic nature of the optical transitions is preserved despite the alloy broadening.
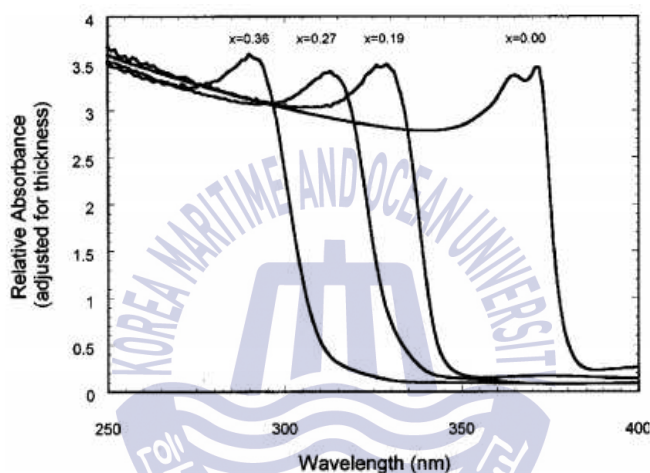
Fig. 2.4 Absorption spectra for $Mg_xZn_{1-x}O$ thin films at room temperature [23]

Moreover, the incorporation of Mg into ZnO moves the conduction band edge up in energy and potentially away from the intrinsic shallow donor state, thus increasing the activation energy of the defect donors and decreasing the effect donor carrier concentration [24]. Moreover, the theoretical formation energy of oxygen vacancy in MgO (rock salt structure) and ZnO (wurtzite structure) are 5.8 eV and 3.1 eV, respectively. The standard electrode potential of Mg is -2.37 E_0/V, while Zn is -0.76 E_0/V. The Mg-O bind does not form the oxygen vacancies easily and Mg could be more easily oxidized than Zn. So the incorporation of Mg into ZnO could be expected to reduce the formation of oxygen vacancies.

2.4 Application of $Mg_xZn_{1-x}O$

$Mg_xZn_{1-x}O$, with tunable bandgap from 3.37 eV to 7.8 eV which covers a broad portion of the ultraviolet spectrum, is a promising candidate for the applications in UV optoelectronic devices such as light emitting diodes, ultraviolet (UV) photodetectors (PDs) and photovoltaic (PV) devices [25-27]. Photodetectors play an important role in monitoring UV radiations that are harmful for human health. In addition to biological and chemical sensors, UV photodetectors have prominent applications in the field of high temperature fire detection, optical communications, calibration of emitters, missile plume detection, air quality monitoring and so forth [28, 29].

ZnO is a promising optoelectronic material in the field of ultraviolet-light-emitting devices and laser diodes, owing to its wide band gap and high exciton binding energy at room temperature. In order to get high illumination intensity and improve the illumination efficiency, $Mg_xZn_{1-x}O/ZnO$ heterojunction is widely used.

$Mg_xZn_{1-x}O$ thin films have high transmittance in the visible region and high electrical conductivity which can be easily controlled by doping, it can be applied for electrode and window material of solar cells. What's more, it's an ideal candidate for the application of solar cells which can be equipped on space satellites result from its lower damage of irradiation in high-irradiation environments [30]. In addition, $Mg_xZn_{1-x}O$ also can be used in piezoelectric devices, such as voltage generates, sensors, transducers and actuators, owing to its large piezoelectric constant [31].

– 9 –

2.5 Metal-Semiconductor contacts

2.5.1 MS interface formation theory

The metal-semiconductor (MS) contact plays a very important role of one kind or another in all solid-state devices. When in the form of a non-rectifying or ohmic contact, it is the critical link between the semiconductor and the outside world. The rectifying MS contact, referred to as the Schottky diode or the MS diode, is found in a number of device structures and is on important device in its own right. Physically and functionally, there are close similarities between the MS diode and the asymmetrical (p+-n or n+-p) step junction diode. Indeed, a large portion of the pn diode analysis can be applied directly to the MS diode with only minor modifications.

An ideal MS contact has the following properties: (1) The metal and semiconductor are assumed to be in intimate contact on an atomic scale, with no layers of any type (such as an oxide) between the components. (2) There is no interdiffusion or intermixing of the metal and semiconductor. (3) There are no adsorbed impurities or surface charges at the MS interface [32]. The ideal MS interface formation theory is described as follows.

2.5.1.1 Schottky diode

The first practical semiconductor device was the metal-semiconductor contact in the form of a point contact rectifier, that is, a metallic whisker pressed against a semiconductor. The device found many applications beginning in 1904. In 1938, Schottky, suggested that the rectifying behavior could arise from a potential barrier as a result of the stable space charges in the semiconductor [33]. The model arising from this concept is known as the Schottky diode. To form the Schottky contact to the n-type semiconductor, the work function of metal (Φ_m) should be larger than that of n-type semiconductor (Φ_s). On the contrary, to form the Schottky contact to p-type semiconductor, Φ_m should be lower than Φ_s.

Suppose now the $\Phi_m > \Phi_s$ metal and n-type semiconductor are brought together to form an ideal MS contact. Consequently, a short time after the conceptual contact formation, electrons will begin transferring from the semiconductor to the metal. The net loss of electrons from the semiconductor creates a surface depletion region and a growing barrier to electron transfer from the semiconductor to the metal. This will continue until the transfer rate across the interface is the same in both directions and the Fermi lever (E_F) is the same throughout the structure. The net result, the equilibrium energy band diagram for an ideal $\Phi_m > \Phi_s$ metal to n-type semiconductor contact, is shown in Figure 2.5 (a).

The semiconductor is taken to be grounded and V_a applied to the metal. The current I is defined to be positive when current flows from the metal to the semiconductor. Applying $V_a > 0$ lowers E_{Fm} below E_{Fs}, reduces the barrier seen by electrons in the semiconductor, and therefore permits a net flow of electrons from semiconductor to the metal, as in Figure 2.5 (b). Even though, the recombination and hole-injection currents still exist. Electron injection from the semiconductor into the metal routinely dominates the observed current. So increasing V_a leads to a rapidly rising forward bias current, since an exponentially increasing number of electrons from the semiconductor are able to surmount the surface barrier.

Applying $V_a < 0$ raises E_{Fm} above E_{Fs} in Figure 2.5 (c). This all but block the flow of electrons from the semiconductor to metal. Some electrons in the metal will be able to surmount the Φ_B barrier, which totally dominants the observed current. The reverse-bias hole diffusion current and the R-G current associated with carrier generation in the depletion region are typically negligible. Reflecting the fact that minority carriers in the semiconductor normally play an insignificant role in determining the *I-V* and other characteristics, the Schottky diode is often said to be a "majority carrier device". Since Φ_B is ideally the same for all reverse bias, the reverse current is expected to remain constant after the reverse bias exceeds a few kT/q volts.
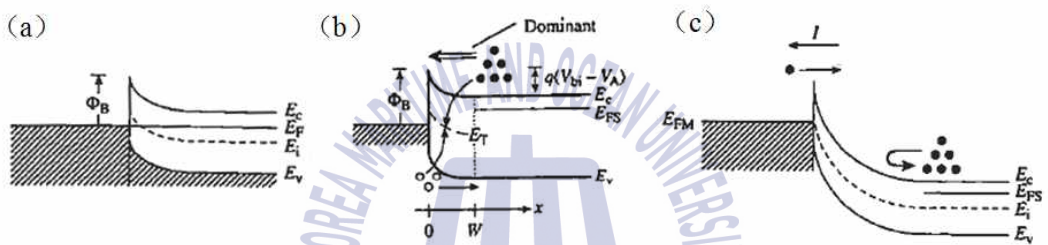
Fig. 2.5 Energy band diagrams for Schottky diode based on n-type semiconductor under (a) flat band (equilibrium), (b) forward bias ($V_a>0$), and (c) forward bias ($V_a<0$) conditions [33]

2.5.1.2 Ohmic contact

Metal-semiconductor contacts can also be non-rectifying; that is, the contact has a negligible resistance relative to the bulk or series resistance of the semiconductor regardless of the polarity of the applied voltage. This type of contact is called an ohmic contact. An ohmic contact means that current flow occurs readily, independent of which voltage polarity is applied to the metal, and an ohmic contact is ideally characterized by a linear (non-rectifying) current-voltage curve. To form the ohmic contact to the n-type semiconductor, the work function of metal (Φ_m) should be lower than that of n-type semiconductor (Φ_s). On the contrary, to form the Schottky contact to p-type semiconductor, Φ_m should be larger than Φ_s. Figure 2.6 shows the energy band diagrams of ohmic contact to n-type semiconductor.
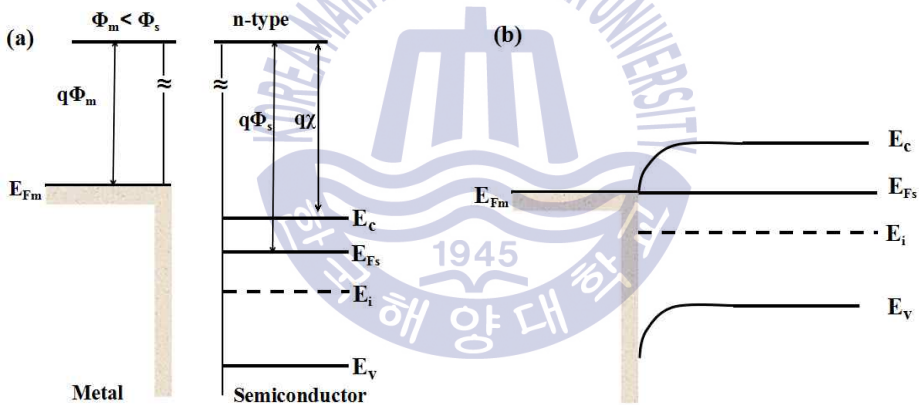
Fig. 2.6 Energy band diagrams for ohmic contact to on n-type semiconductor under (a) isolated and (b) flat band (equilibrium) conditions

2.5.2 Schottky diode current-voltage characteristics

The Schottky diode interface formation theory is discussed in chapter 2.5.1. For Schottky diodes operated at moderate temperature (e.g., 300 K), the dominate transport mechanism is thermionic emission of majority carriers from the semiconductor over the potential barrier into the metal. According to the thermionic emission (TE) theory the current−voltage characteristic with the series resistance is given as follows [34]:

$$I = I_0 \left[\exp\left(\frac{q(V - IR_S)}{nkT} \right) - 1 \right]$$
(2.1)

where q is the electron charge, n is the ideality factor, k is the Boltzmann constant, R_s is the series resistance, T is the absolute temperature and I_0 is the saturation current which is given by

$$I_0 = AA^* T^2 \exp\left(-\frac{q\Phi_B}{kT} \right)$$
(2.2)

where Φ_B is the Schottky barrier height, A is the area of the diode, and A* is the effective Richardson constant.

According to the San-Noyce-Shockley theory [35], the diode's ideality factor is 1.0 at low voltage and 2.0 at high voltage [36]. But, at the wide band gap material, the ideality factors were reported more higher [37, 38]. This is because besides the recombination occurs via band to band and traps in the bulk areas from the device, there are other recombination occurring in other ways or in other areas of device which make the ideality factor deviate from the ideal. For diode ideality factor (n), the current in a forward biased Schottky diode is generally described by the equation which is not affected by series resistance at low voltage.

$$I = I_0 \left[\exp\left(\frac{qV}{nkT} \right) - 1 \right]$$
(2.3)

At room temperature (300 K), kT/q is 0.0259 eV. For the applied voltage greater than a few kT/q volt, the -1 can be removed for simplify the equation,

$$I = I_0 \left[\exp\left(\frac{qV}{nkT} \right) \right] \tag{2.4}$$

Taking the logarithms of both sides of the equation,

$$\ln(I) = \ln(I_0) + \frac{qV}{nkT} \tag{2.5}$$

Thus a plot of the natural logarithm diode current versus voltage should be straight line with slop   and a y-axis intercept of $\ln(I_0)$.

I_0 can be derived from the straight line intercept of $\ln(I)$ at $V=0$ and ideality factor n is determined from the slope of the liner region of the forward bias ln $(I)-V$ curve.

Schottky and Mott developed the basic theory of Schottky contact formation [33]. This predicts that for a n-type semiconductor, where Φ_B is the Schottky barrier height (SBH) of an "ideal" homogeneous contact, Φ_m is the metal work function, and is the electron affinity of the semiconductor. In practice, most semiconductors have a much weaker dependence of SBH on Φ_m. That is the experimental barrier height deviates from the ideal value. These two reasons can illustrate this deviation: (1) a Schottky barrier junction includes a termination of the semiconductor crystal which can lead to charges at the metal-semiconductor due to incomplete covalent bonds and other effects; (2) the contact is seldom an atomically sharp discontinuity between the semiconductor crystal and the metal which results in a thin interfacial layer which is neither semiconductor nor metal [39]. In consideration of the surface states, the interfacial layer, microscopic clusters of metal-semiconductor phases, and other effects, the measured barrier heights are used in device design. The effective barrier height Φ_B can be determined from equation (2.2) and can be written as

$$\Phi_B = \frac{kT}{q} ln\left(\frac{AA^* T^2}{I_0} \right) \tag{2.6}$$

The series resistance R_S is influenced by the presence of the interface layer between the metal and semiconductor and leads to non-ideal forward bias

current-voltage plots. When the applied voltage is sufficiently large where, the effect of the R_S can be seen at the non-linear regions of the forward bias $I\mathrm{-}V$ characteristics. In this case, the series resistance is given by the tangent to the $I\mathrm{-}V$ curve. Equation (2.1) can be re-written as taking the logarithms of both sides of the equation,

$$\ln(I) = \ln(I_0) + \frac{q(V - IR_S)}{nkT} \tag{2.7}$$

The $\ln(I_0)$ value is so small than $\ln(I)$ that $\ln(I_0)$ can be neglected. Solving the equation for V and then differentiating V with respect to I yields

$$I\frac{dV}{dI} = IR_S + \frac{nkT}{q} \tag{2.8}$$

Thus a plot of versus forward current at high voltage is straight line and slope means the series resistance.

Chapter 3. Experiment and analysis methods

3.1 Experiment methods

3.1.1 Theory of RF magnetron sputter system

Sputter deposition is a physical vapor deposition process for depositing thin films, sputtering means ejecting material from a target and depositing it on a substrate such as a silicon wafer. The target is the source material. Substrates are placed in a vacuum chamber and are pumped down to a prescribed process pressure. Sputtering starts when a negative charge is applied to the target material causing a plasma or glow discharge. Positive charged gas ions generated in the plasma region are attracted to the negatively biased target plate at a very high speed. This collision creates a momentum transfer and ejects atomic size particles form the target. These particles are deposited as a thin film into the surface of the substrates.

Magnetron are used to increase the percentage of electrons that take part in ionization of events and thereby increase the probability of electrons striking the Argon atoms, increase the length of the electron path, and hence increase the ionization efficiency significantly. Magnetron sputtering can be done either in direct current (DC) or radio frequency (RF) modes. DC sputtering is done with conducting materials. If the target is a non-conducting material the positive charge will build up on the material and it will stop sputtering. RF sputtering can be done both conducting and non-conducting materials.

3.1.2 Deposition of ZnO and $Mg_xZn_{1-x}O$ thin films

The ternary $Mg_xZn_{1-x}O$ thin films were deposited on n-Si (100) substrates by RF magnetron co-sputtering, as shown in Figure 3.1. Silicon substrates yield a resistivity of 0.5-8 $\Omega \cdot cm$ in conjunction with an n-type carrier. The co-sputtered commercial targets, ZnO and $Mg_{0.3}Zn_{0.7}O$ (4 inch in diameter, Mg/(Mg+Zn), 30 at.%), had purity of 99.99 %. Before loading into the sputtering chamber, the Si substrates were cleaned with acetone, methanol, and de-ionized water in an ultrasonicator for 15 min. The base pressure was less than 10^{-6} Torr, and the working pressure was 5 mTorr. Argon gas was introduced at a flow rate of 20 cm^3/min, which was controlled by using a mass flow controller. The RF power of ZnO target was 100 W, which was remained unchanged, whereas the power applied at $Mg_{0.3}Zn_{0.7}O$ target was set to 50 W, 100 W and 150 W. The ZnO and $Mg_xZn_{1-x}O$ films were deposited for 90 min at 300 ℃. The deposition condition is summarized in Table 3.1. For convenience, each $Mg_xZn_{1-x}O$ thin film is numbered as follows, as shown in Table 3.2: the ZnO (100W) co-sputtered with $Mg_{0.3}Zn_{0.7}O$ (50, 100, and 150 W) are designated as MZO50, MZO100, and MZO150, respectively. The sample deposited by using single ZnO (100W) and $Mg_{0.3}Zn_{0.7}O$ (100W) are designated as ZnO and MgZnO, respectively. After deposition, all the samples were annealed at 750 ℃ in O_2 ambient for 60 min.
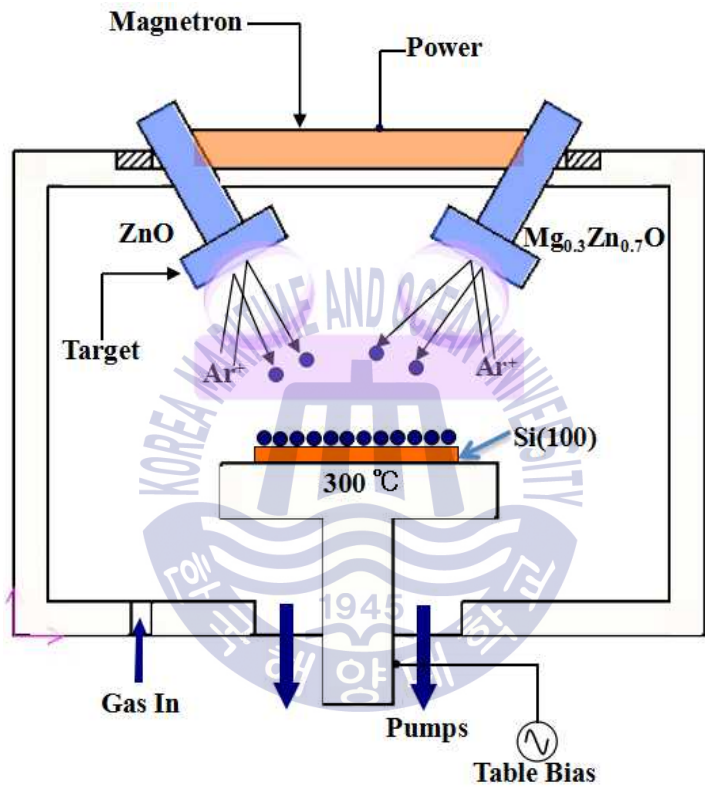
Fig. 3.1 Schematic representation of RF magnetron co-sputtering system

Table 3.1 The deposition conditions of RF magnetron co-sputtering for ZnO and $Mg_xZn_{1-x}O$ thin films

System	RF-co magnetron sputter
Target	ZnO (4"), MgZnO (30 at.%;4")
ZnO power(w)	100 (fixed)
$Mg_{0.3}Zn_{0.7}O$ power(w)	0, 50, 100, 150
Base pressure(Torr)	6.60E-06
Working pressure(mTorr)	5
Gas	Ar (20 sccm)
Deposition Temp.	300℃
Deposition Time	1.5h
Substrate	Si（100）

Table 3.2 The sample names according to the deposition conditions

Samples name	Deposition Conditions
ZnO	Single ZnO target
MZO50	ZnO 100W + $Mg_{0.3}Zn_{0.7}O$ 50W
MZO100	ZnO 100W + $Mg_{0.3}Zn_{0.7}O$ 100W
MZO150	ZnO 100W + $Mg_{0.3}Zn_{0.7}O$ 150W
MgZnO	Single $Mg_{0.3}Zn_{0.7}O$ target 100W

3.1.3 Fabrication of Ti/Au electrodes on ZnO and $Mg_xZn_{1-x}O$ thin films

The patterns of transmission line model (TLM) was formed by using the photolithography method. The Ti (10 nm)/Au (50 nm) contact were deposited by using the e-beam evaporation system in Figure 3.2, and after that the patterns were finally completed by the lift-off method. The flow chart for process steps is shown in Figure 3.3. To form ohmic contact the Ti (10 nm)/Au (50 nm) contact metals were post-annealed at 500 ℃ in vacuum for 60 s by rapid thermal process.
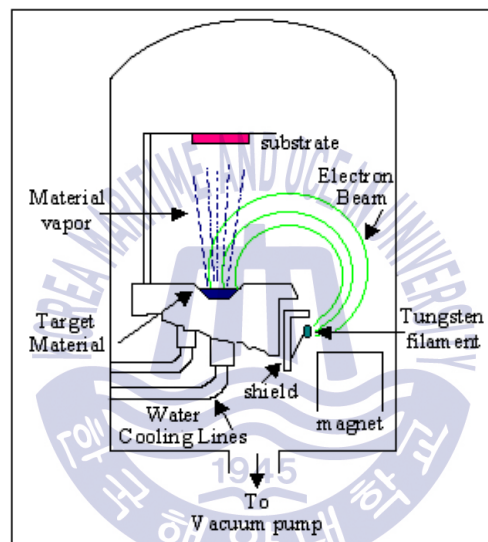
Fig. 3.2 Schematic representation of e-beam deposition system
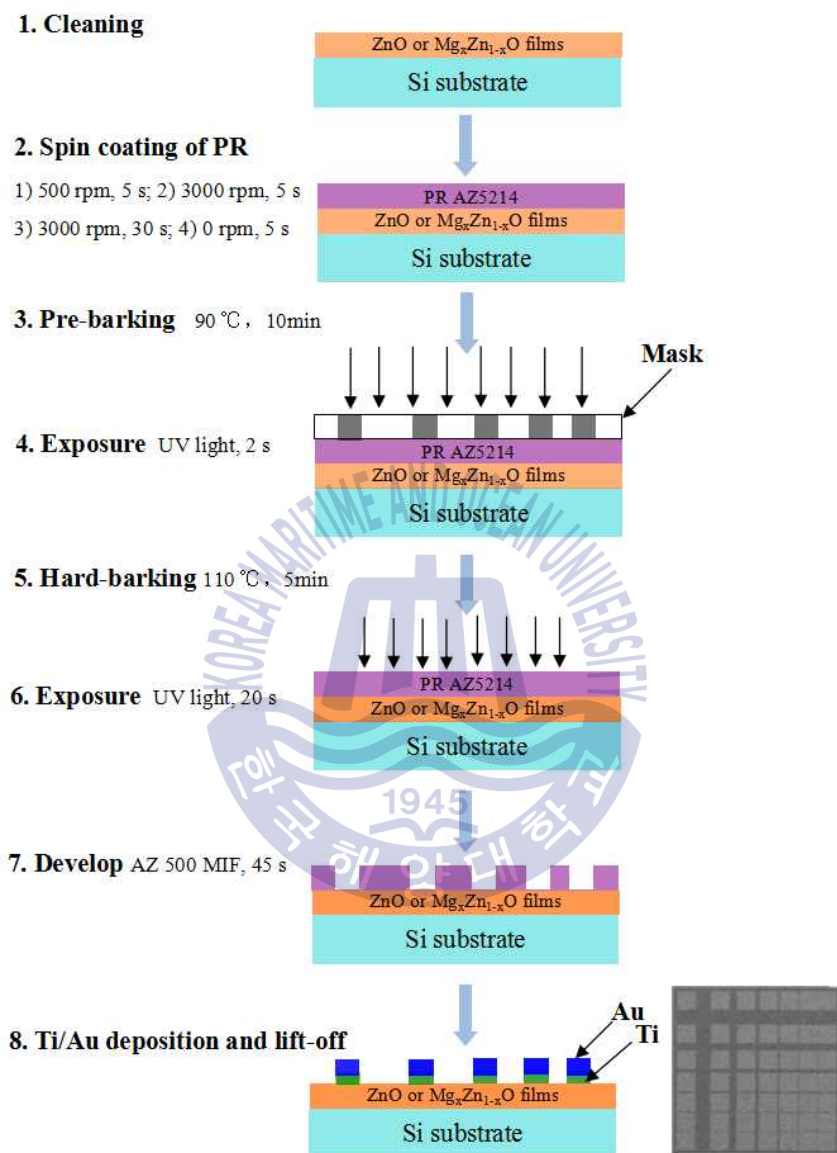
Fig. 3.3 Flow charts of the fabrication process of TLM electrodes

3.2 Analysis methods

The Mg concentration was confirmed by energy dispersive X-ray spectrum (EDS, Tescan, MIRA-3). The structure characteristics were investigated by the X-ray diffraction (XRD, Rigaku, Smartlab) spectrum. The surface morphologies were characterized by the atomic force microscopy (AFM, Park systems, XE-100). The *I-V* characteristics were evaluated by the semiconductor parameter analysis (Hewlett-Packard, HP-4145B). The electrical properties were measured by Hall effect measurement (Ecopia, HMS-5000).

3.2.1 X-ray diffraction

X-ray diffraction (XRD) relies on the dual wave/particle nature of X-rays to obtain information about the structure of crystalline materials. A primary use of the technique is the identification and characterization of compounds based on their diffraction pattern. X-rays have wavelengths on the order of a few angstroms (a angstrom = 0.1 nm). This is the typical inter-atomic distance in crystalline solid, making X-rays the correct order of magnitude for diffraction of atoms of crystalline materials.

The dominant effect that occurs when an incident beam of monochromatic X-rays interacts with a target material is scattering of those X-rays from atoms within the target material. In materials with regular structure (i.e. crystalline), the scattered X-rays undergo constructive and destructive interference. The diffraction of X-rays by crystals is described by Bragg's Law (Eq. 3.1). The directions of possible diffractions depend on the size and shape of the unit cell of the material. The intensities of the diffracted waves depend on the kind and arrangement of atoms in the crystal structure.

$$2d\sin\theta = n\lambda \tag{3.1}$$

where, λ is wavelength of X-rays, Θ is scattering angle, d is inter-plane distance of (i.e atoms, ions, molecules), and n is the integer representing the order of the diffraction peak.
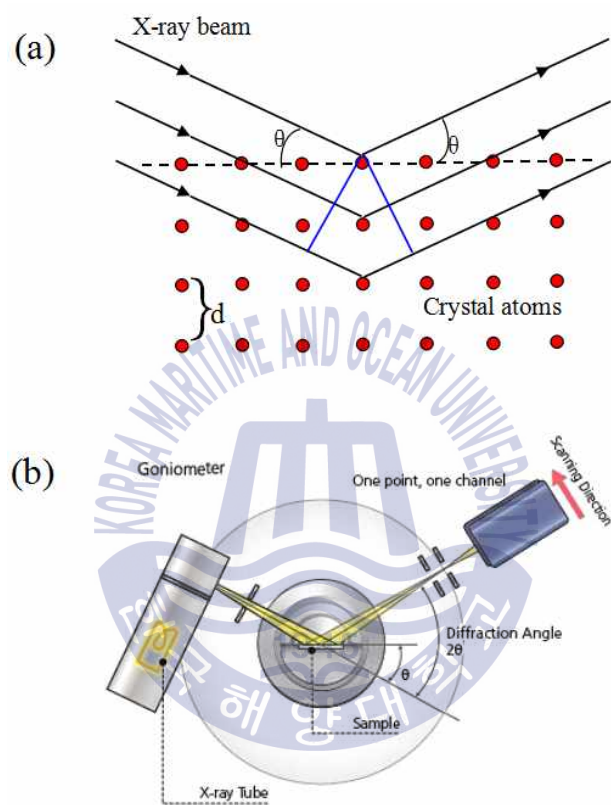
Fig. 3.4 (a) The principle of X-ray diffraction, (b) X-ray diffraction diagram

3.2.2 Atomic force microscope

Atomic force microscope (AFM) is a high-resolution imaging technique that can resolve features as small as an atomic lattice in the real space. AFM has much broader potential and application because it can be used for imaging any conducting or non-conducting surface. AFM works by bringing a cantilever tip in contact with the surface to be imaged as shown in Figure 3.5. An ionic repulsive force from the surface applied to the tip bends the cantilever upwards. The amount of bending, measured by a laser spot reflected on to a split photo detector, can be used to calculate the force. By keeping the force constant while scanning the tip across the surface, the vertical movement of the tip follows the surface profile and is recorded as the surface topography by the AFM.
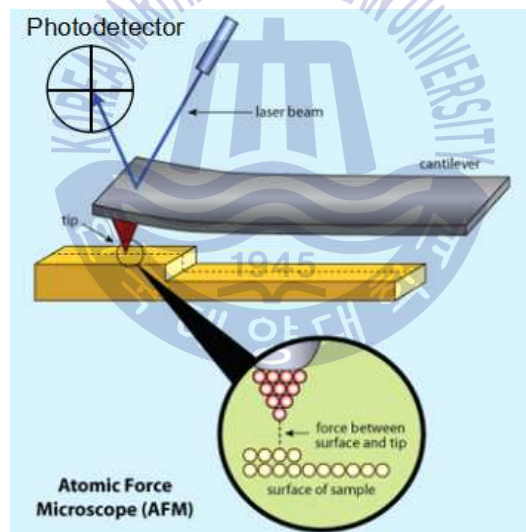
Fig. 3.5 The schematic of AFM measurement

3.2.3 EDS (Energy-dispersive X-ray spectroscopy)

Energy-dispersive X-ray spectroscopy (EDS, EDX, or XEDS), sometimes called energy-dispersive X-ray analysis (EDXA) or energy dispersive X-ray microanalysis (EDXMA), is an analytical technique used for the elemental analysis or chemical characterization of a sample. Interaction of an electron beam with a sample target produces a variety of emissions, including X-rays as shown in Figure 3.6. An EDS detector is used to separate the characteristic X-rays of different elements into an energy spectrum, and EDS system software is used to analyze the energy spectrum in order to determine the abundance of specific elements. EDS can be used to find the chemical composition of materials down to a spot size of a few microns, and to create element composition maps over a much broader raster area. Together, these capabilities provide fundamental compositional information for a wide variety of materials.
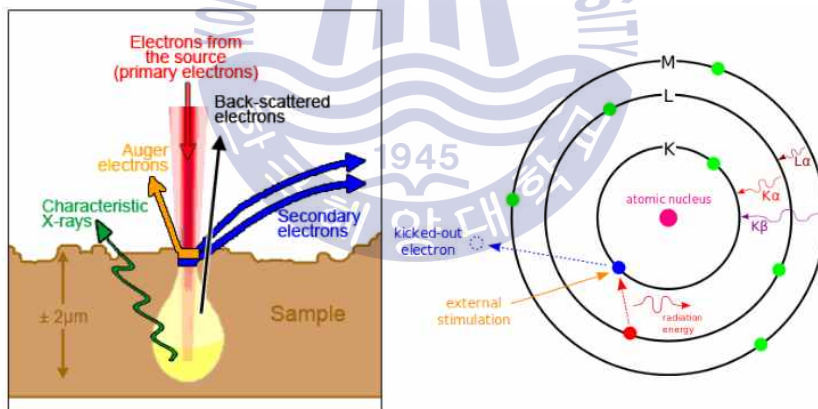
Fig. 3.6 The principle of EDS measurement

3.2.4 4145B Semiconductor parameter analyzer

HP 4145B semiconductor parameter analyzer is an extremely useful tool for characterizing semiconductor devices in conjunction with LabVIEW. HP 4145B semiconductor parameter analyzer is divided into two parts. These two parts are applying a voltage to semiconductor device, and reading the measured current for transmitting back to the LabVIEW. The basic principle of HP 4145B semiconductor parameter analyzer is shown in Figure 3.7.
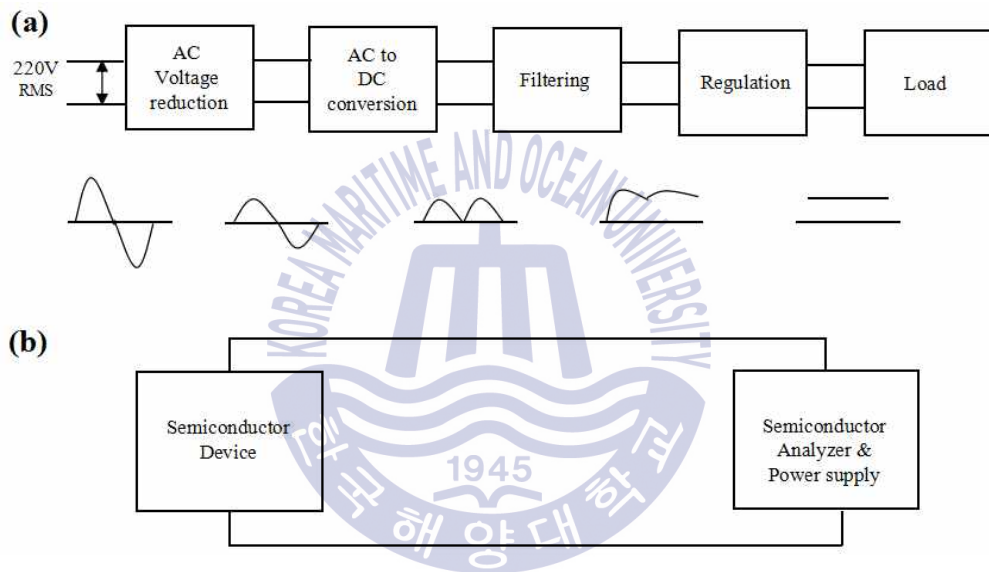
Fig. 3.7 The principle of HP 4145B semiconductor parameter analyzer

(a) Power supply unit and (b) wiring to semiconductor

3.2.5 Hall effect measurement

HMS-5000 Hall effect measurement system is widely used to measure electrical properties of semiconductors. It relies on the van der Pauw technique which is a combination of resistivity measurement and Hall measurement. The basic physical principle underlying the Hall effect is the Lorentz force, which is a combination of two separate forces: the electric force and the magnetic force as shown in Figure 3.8 (a). The measurement sketch of van der Pauw is shown in Figure 3.8 (b). The objective of the Hall measurement in the van der Pauw technique is to determine the sheet carrier density n_s (n_s=nd) by measuring the Hall voltage V_H according to the equation

$$n_s = IB/q \left| V_H \right| \tag{3.2}$$

where I is the current, B is the magnetic field, d is the sample thickness, and q is the elementary charge.

Then through the van der Pauw equation

$$\exp\left(-nR_A/R_s\right) + \exp\left(-nR_B/R_s\right) = 1 \tag{3.3}$$

the sheet resistance R_s can be solved. The bulk electrical resistivity ρ can be calculated using $\rho = R_s d$.

Finally, we can determine the Hall mobility from the equation

$$\mu = \left| V_H \right| / R_s IB = 1/q n_s R_s \tag{3.4}$$
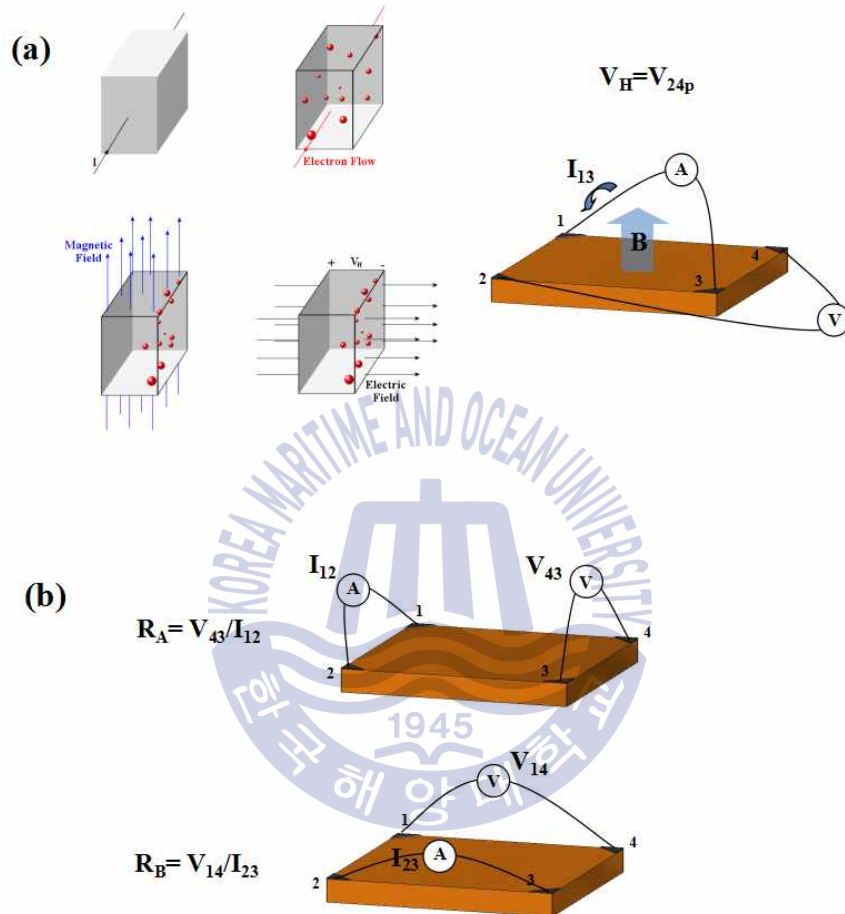
Fig. 3.8 The principle of van der Pauw measurement (a) Hall measurement and (b) resistivity measurement

Chapter 4. Results and discussions

4.1 Structural and electrical properties of $Mg_xZn_{1-x}O$ thin films

4.1.1 Results and discussions

4.1.1.1 The structural properties of $Mg_xZn_{1-x}O$ films as the function of Mg content

The Mg concentrations of $Mg_xZn_{1-x}O$ films were confirmed by EDS measurement. The Mg compositions, the ratio of Mg/(Mg+Zn) at.%, in MZO50, MZO100, and MZO150 are 2 at.%, 11 a.t%, and 18 at.%, respectively (as shown in Figure 4.1). With the increasing in RF power of $Mg_{0.3}Zn_{0.7}O$ target, more plasma particles strike the $Mg_{0.3}Zn_{0.7}O$ target and eject more MgZnO atoms to the Si substrate. So the Mg content of $Mg_xZn_{1-x}O$ film increases as the RF power of $Mg_{0.3}Zn_{0.7}O$ target increases. The thickness of ZnO, MZO50, MZO100, and MZO150 films measured by SEM are 180 nm, 260 nm, 310 nm, and 330 nm, respectively. The XRD diffraction patterns of ZnO, $Mg_{0.02}Zn_{0.98}O$, $Mg_{0.11}Zn_{0.89}O$, and $Mg_{0.18}Zn_{0.82}O$ are shown in Figure 4.2 (a).

According to Figure 4.2 (a), all samples predominantly show the (002) direction with hexagonal wurtzite structure and no phase separation. The ZnO (002) diffraction peak is 34.5° whereas the $Mg_{0.02}Zn_{0.98}O$, $Mg_{0.11}Zn_{0.89}O$, and $Mg_{0.18}Zn_{0.82}O$ thin films display hexagonal MgZnO (002) peak at 34.5°, 34.58°, and 34.66°, which shifts to the 34.74° observed for single $Mg_{0.3}Zn_{0.7}O$ target (as shown in Figure 4.2 (b)). This indicates an increase in the incorporation of Mg into ZnO, which is consistent with the EDS result. According to Figure 4.2 (b), the full widths at half maxima (FWHM) of $Mg_xZn_{1-x}O$ thin films increases as the Mg concentration increases owing to the difference between the Mg^{2+} and Zn^{2+} ionic radiuses. Even the incorporation of Mg into ZnO degrades the crystalline quality, the FWHM value of $Mg_{0.18}Zn_{0.82}O$ film (0.17°) which is much smaller than that of $Mg_{0.16}Zn_{0.84}O$ film (0.28°) deposited on silicon substrate by magnetron sputtering with single $Mg_{0.16}Zn_{0.84}O$ target [40]. This exhibits the $Mg_xZn_{1-x}O$ thin films in our experiment own relatively higher crystalline quality.

Figure 4.3 shows the AFM results of $Mg_xZn_{1-x}O$ thin films. The surfaces of the $Mg_xZn_{1-x}O$ thin films reveal grain-shaped islands. The value of the root-mean-square (RMS) roughness is from 4.5 nm to 7.6 nm. With the increasing in Mg content, the grain size increases from 75.2 nm to 89.7 nm.
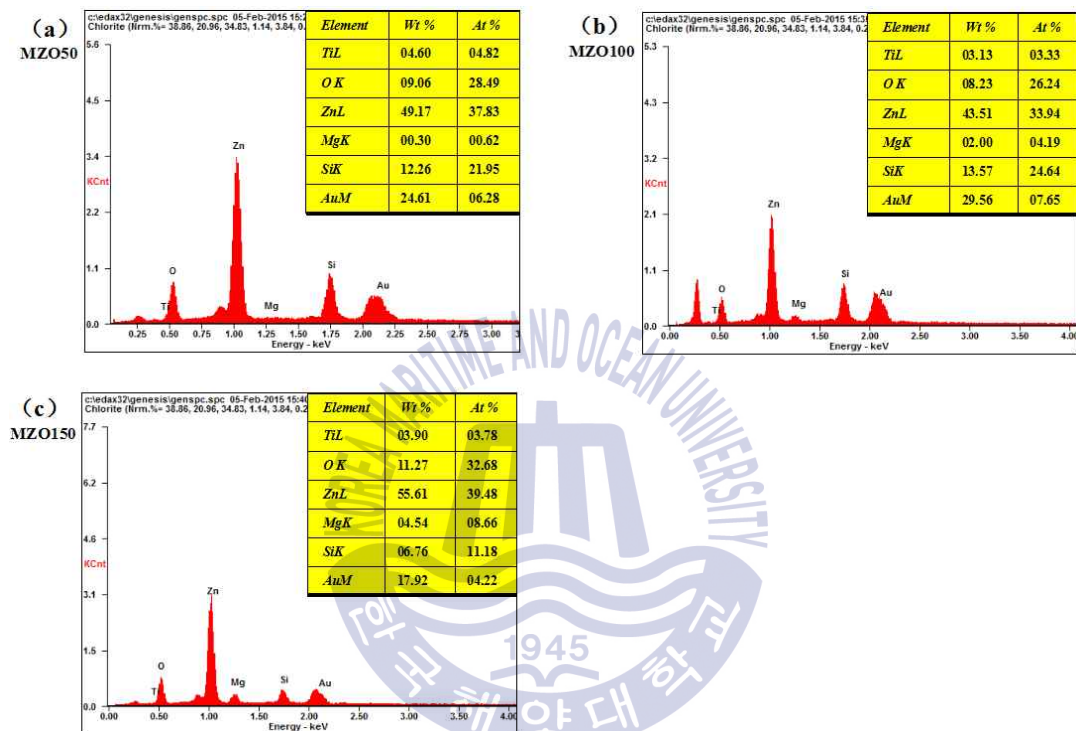
Fig. 4.1 EDS spectrum for (a) MZO50, (b) MZO100, and (c) MZO150 thin films annealed at 750 ℃ for 60 min
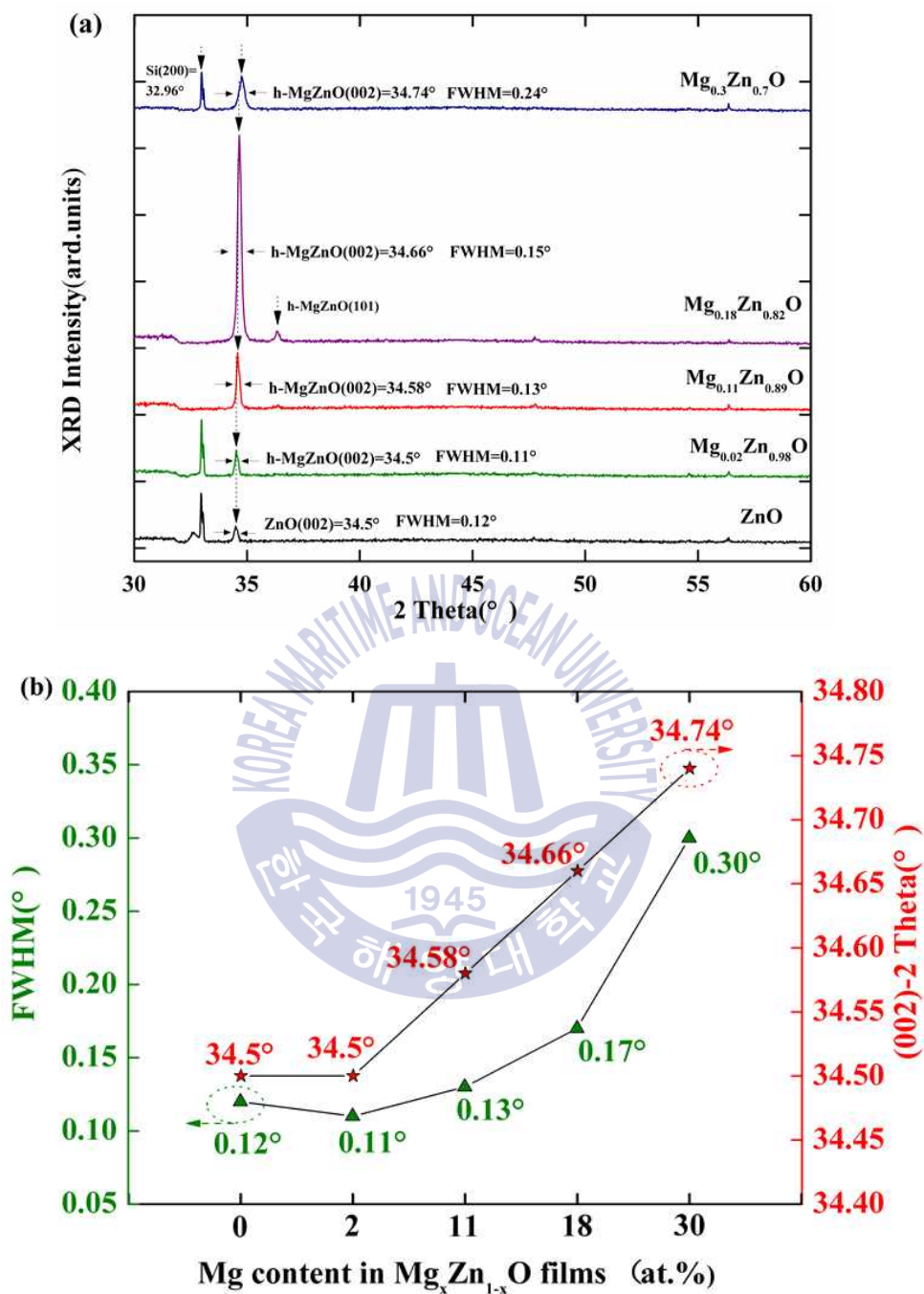
Fig. 4.2 (a) XRD θ-2θ patterns for ZnO, $Mg_{0.02}Zn_{0.98}O$, $Mg_{0.11}Zn_{0.89}O$, $Mg_{0.18}Zn_{0.82}O$, and $Mg_{0.3}Zn_{0.7}O$ thin films annealed at 750 ℃ for 60 min, and (b) XRD results versus the Mg concentration

ZnO

RMS roughness: 4.5 nm
Grain size: 79.9 nm

Mg$_{0.02}$Z$_{0.98}$O

RMS roughness: 7.6 nm
Grain size: 75.2 nm

Mg$_{0.11}$Z$_{0.89}$O

RMS roughness: 6.2 nm
Grain size: 83.7 nm

Mg$_{0.18}$Z$_{0.82}$O

RMS roughness: 6.3 nm
Grain size: 89.7 nm
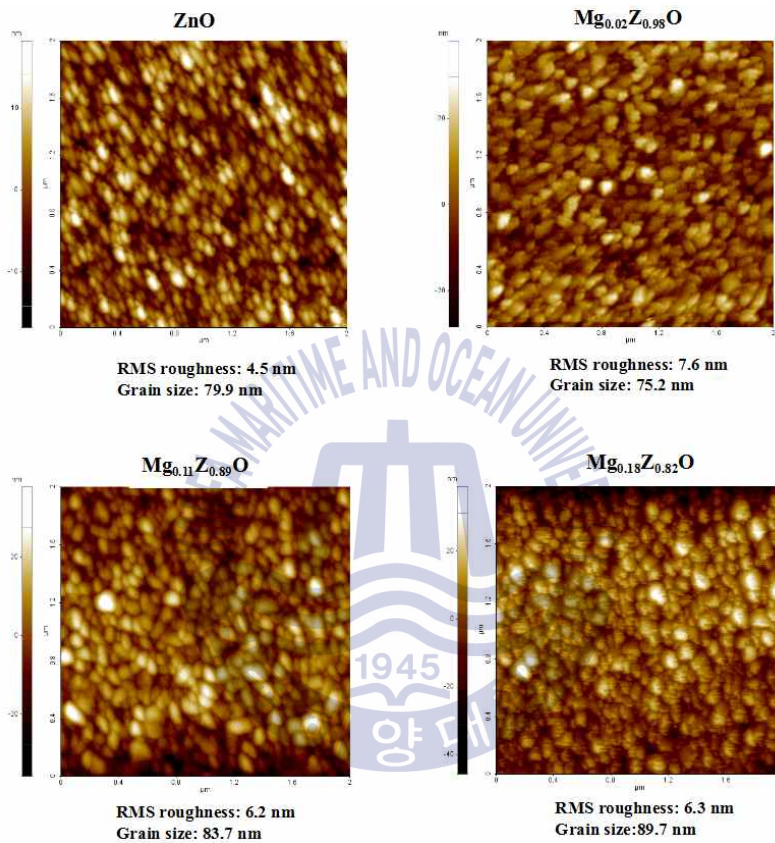
Fig. 4.3 Surface morphologies (2×2 μm^2) of ZnO and Mg$_x$Zn$_{1-x}$O thin films annealed at 750 ℃ for 60 min

4.1.1.2 The electrical properties of $Mg_xZn_{1-x}O$ films as the function of Mg content

Figure 4.4 shows the *I-V* characteristics measured by using the TLM method with a series of Ti/Au contacts (200 μm × 200 μm) with different spacings (d_i = 10, 20, 40, and 80 μm). The Ti/Au metal on ZnO, $Mg_{0.02}Zn_{0.98}O$, $Mg_{0.11}Zn_{0.89}O$, and $Mg_{0.18}Zn_{0.82}O$ all show linear *I-V* curves indicating the ohmic contact properties.

Figure 4.5 shows the resistance as the function of distance between two adjacent contacts measured by using TLM method. The resistance was calculated according to the *I-V* curves (-5 V~5 V) in figure 4.4 and the straight line in figure 4.5 was fitted by the linear square method. According to the TLM method [41. 42], the total resistance, R, between two adjacent contacts is given by Eq.(4.1):

$$R(d_i) = 2R_c + \frac{R_s}{W}d_i \tag{4.1}$$

where R_c denotes the contact resistance, W the width of the contact, and R_s the sheet resistance of the semiconductor layer outside the contacts. Thus, the special contact resistivity can be obtained by Eq.(4.2):

$$\rho_c = \frac{R_c^2 W^2}{R_s} \tag{4.2}$$

and the bulk film resistivity can be evaluated by Eq.(4.3) :

$$\rho = R_s \cdot h \tag{4.3}$$

where h denotes the thickness of $Mg_xZn_{1-x}O$ thin films.

Figure 4.6 shows the electrical properties of $Mg_xZn_{1-x}O$ thin films as the function of Mg content. The special contact resistivity increases from 1.79×10^{-2} $\Omega \cdot cm^2$ to 1.34 $\Omega \cdot cm^2$ as the Mg concentration increase from 0at% to 18at% in $Mg_xZn_{1-x}O$ thin films. This is because that the incorporation of Mg into ZnO reduces the formation of oxygen vacancies which acting as donors for electrons below the contact. The resistivity of ZnO, $Mg_{0.02}Zn_{0.98}O$, $Mg_{0.11}Zn_{0.89}O$, $Mg_{0.18}Zn_{0.82}O$ films are 8.71×10^{-2} $\Omega \cdot cm$, 2.23×10^{-1} $\Omega \cdot cm$, 2.48 $\Omega \cdot cm$, and 4.25 $\Omega \cdot cm$, respectively. The resistivity increases for the films with the increasing in Mg concentration, which is

consist with Hall effect measurement result (as shown in Figure 4.7). This may result from the substitution of Mg ions with a smaller ionic radius for Zn sites. The increased Mg ion causes more lattice distortion, to some extent, which increases the lattice scattering. Similarly, Chen et al. also has observed an increasing in the resistivity of the Mn doped ZnO with increasing Mn concentration [42].

Figure 4.7 shows the Hall effect measurement result, the electron concentration of ZnO, $Mg_{0.02}Zn_{0.98}O$, $Mg_{0.11}Zn_{0.89}O$, and $Mg_{0.18}Zn_{0.82}O$ are 1.17×10^{19} /cm^3, 2.84×10^{18} /cm^3, 3.14×10^{17} /cm^3, and 1.17×10^{17} /cm^3, which decreases significantly with the increasing in Mg concentration. This indicates that the incorporation of Mg into ZnO reduces the formation of oxygen vacancies due to the strong interaction between Mg^{2+} ions and O^{2-} ions. The similar relation between carrier concentration and oxygen vacancies in $ZnO:Ga_{0.004}$ thin film was found by Lorenz et al. [44]. The decrease of oxygen vacancies which act as donors under the ohmic contact explains why the special contact resistivity increases as the Mg content increases. As the carrier concentration decreases from 1.17×10^{19} /cm^3 to 1.17×10^{17} /cm^3, the Hall mobility increases from 8.11 cm^2/Vs to 15.3 cm^2/Vs. Even though the carrier concentration is reduced to 0.01 times of that of ZnO as the Mg concentration is increased to 18 at.%, the mobility is only increased to 2 times of ZnO, which indicates the incorporation of Mg into ZnO causes the lattice distortion which explains why the resistivity of $Mg_xZn_{1-x}O$ films increases with the increasing in Mg content. Klüpfel et al. [45] has successfully fabricated the MESFET based on ZnO:Mg thin film grown by pulsed laser deposition on a-plane sapphire. In which the Hall mobility of the thin film was 10 cm^2/Vs. In our case, the Hall mobility of $Mg_{0.11}Zn_{0.89}O$ and $Mg_{0.18}Zn_{0.82}O$ are higher than 10 cm^2/Vs. Transistors made from materials with high mobilities generally have better properties than those made from lower mobility material. So the $Mg_xZn_{1-x}O$ ($0 \leq x \leq 0.18$) films display good electrical properties and are promising for the future application in optoelectronic devices.
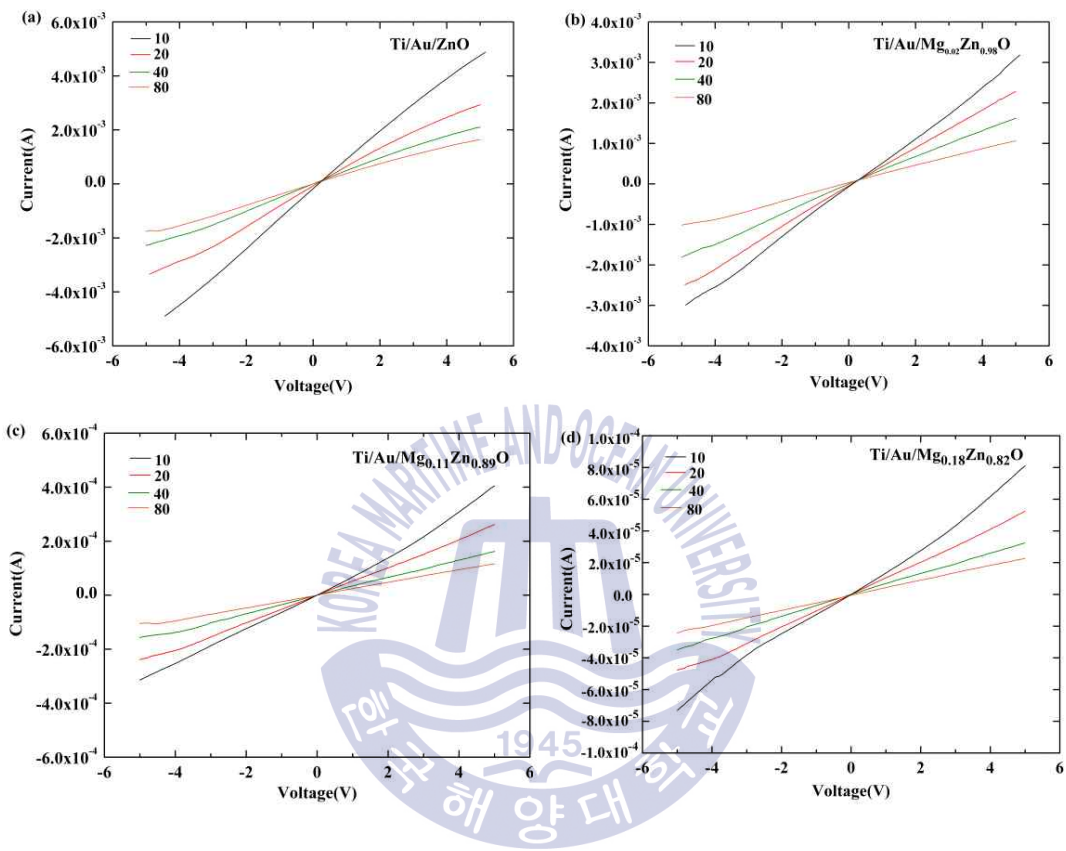
Fig. 4.4 The current-voltage characteristic of Ti/Au contact metal on (a) ZnO, (b) $Mg_{0.02}Zn_{0.98}O$, (c) $Mg_{0.11}Zn_{0.89}O$, and (d) $Mg_{0.18}Zn_{0.82}O$ thin films measured by transmission line model
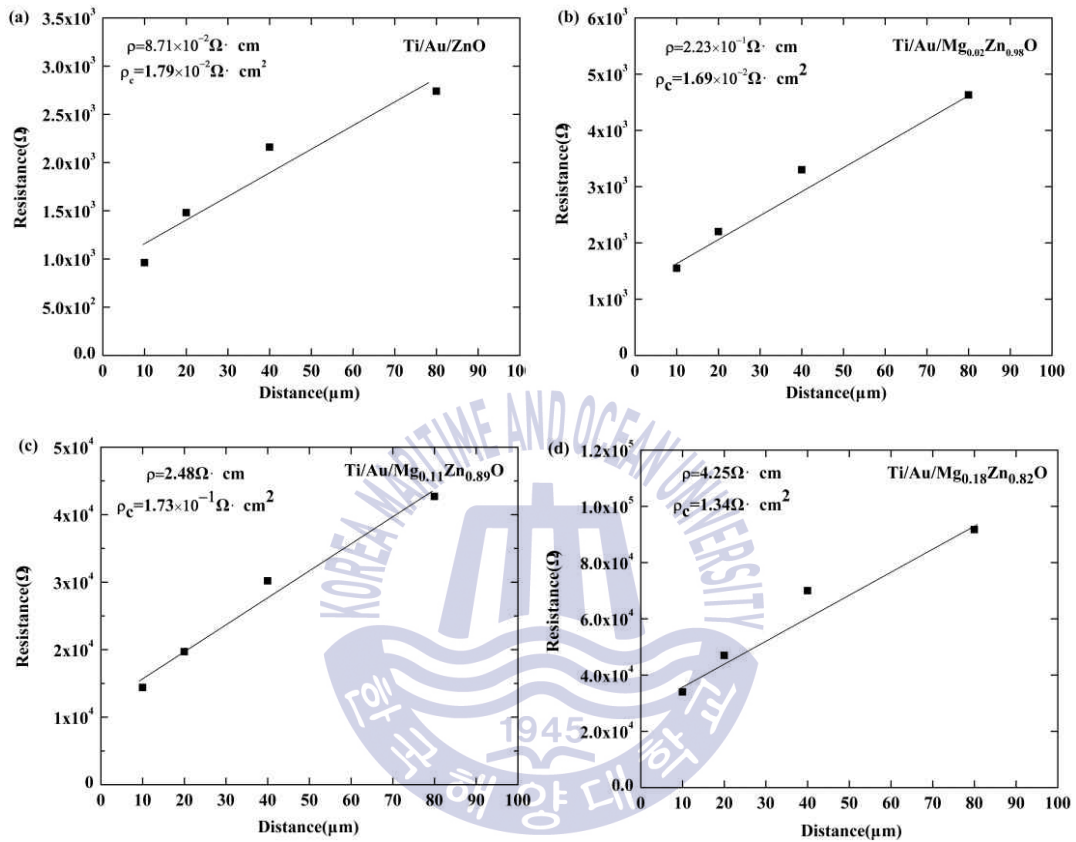
Fig. 4.5 The resistance-distance correlation of Ti/Au contact metal on (a) ZnO, (b) $Mg_{0.02}Zn_{0.98}O$, (c) $Mg_{0.11}Zn_{0.89}O$, and (d) $Mg_{0.18}Zn_{0.82}O$ thin films measured by transmission line model (the resistance is derived from the *I-V* curve in -5V~5V voltage range)
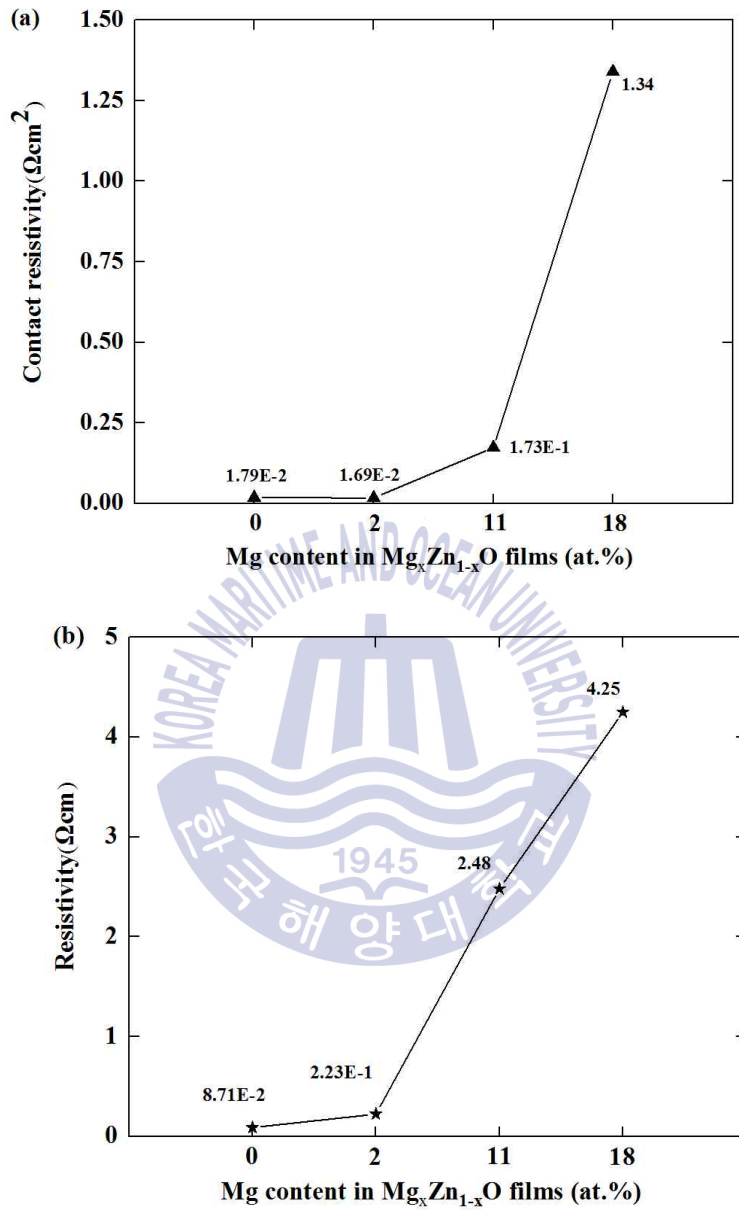
Fig. 4.6 (a) Special contact resistivity and (b) resistivity of $Mg_xZn_{1-x}O$ thin films as the function of Mg concentration measured by transmission line model
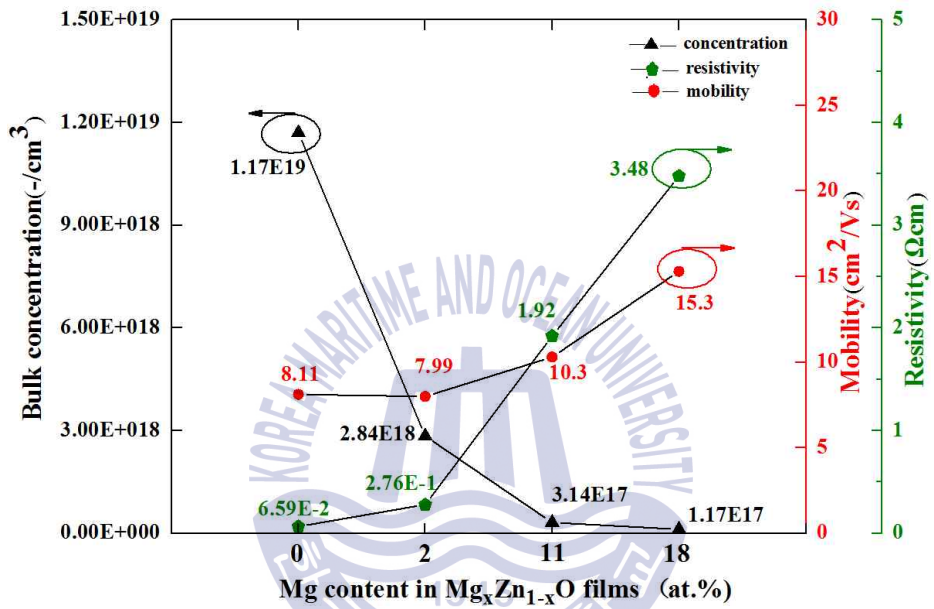
Fig. 4.7 The carrier concentration, mobility and resistivity of $Mg_xZn_{1-x}O$ thin films as function of Mg concentration measured by Hall effect measurement

4.1.2 Conclusions

We successfully deposited the $Mg_xZn_{1-x}O$ films with the maximum Mg content of 18 at.% on Si substrates by RF magnetron co-sputtering with ZnO and $Mg_{0.3}Zn_{0.7}O$ targets. The $Mg_xZn_{1-x}O$ films predominantly showed (002) direction with Hexagonal wurtzite structure and no phase separation. The electrical properties of $Mg_xZn_{1-x}O$ films were tuned by the Mg content. With the increasing in Mg content, the resistivity increased and the carrier concentration decreased from 1.17×10^{19} cm^{-3} to 1.17×10^{17} cm^{-3} indicates the reduction of oxygen vacancies. Meanwhile, the Hall mobility increased as the carrier concentration decreased. The Hall mobility of $Mg_{0.11}Zn_{0.89}O$ and $Mg_{0.18}Zn_{0.82}O$ are 10.3 and 15.3 cm^2/Vs which are higher than the reported value [45]. So the $Mg_xZn_{1-x}O$ ($0 \leq x \leq 0.18$) films own the good-quality structural and electrical properties, which are promising for the future application in optoelectronic devices.
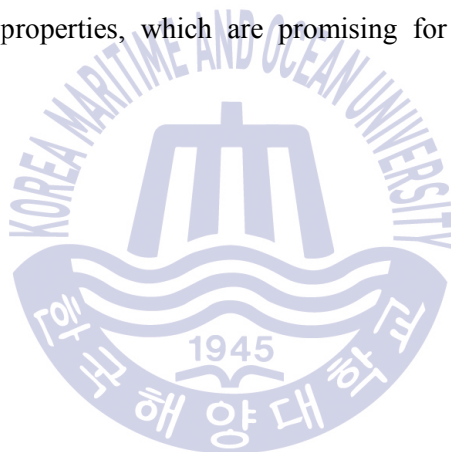
4.2 The electrical properties of $Mg_xZn_{1-x}O$ films based Schottky diodes

4.2.1 The effect of Mg content on electrical properties of $Mg_xZn_{1-x}O$ films based Schottky diodes with Ag metal

4.2.1.1 Motivation

ZnO and its alloys are promising for optoelectronic devices such as light emitting diodes, ultraviolet (UV) photodetectors (PDs) and photovoltaic (PV) devices [25-27]. Recently, $Mg_xZn_{1-x}O$ based Schottky diodes have attracted considerable attention in UV PD and PV applications [26, 27]. The Schottky contacts on ZnO films have been widely investigated, but the Schottky properties are controversial [26]. The performance of Schottky contacts on ZnO is affected by various factors such as native defects [46], the crystal orientation [47], and/or the surface treatment condition [48]. The Fermi level pinning due to the oxygen vacancies near the surfaces has been attributed to the difficulties in reproducing high performance Schottky junctions. Many surface pretreatments such as oxygen plasma treatment [49], hydrogen peroxide (H_2O_2) treatment [50], and post-growth annealing, were reported to improve the rectifying characteristics by reducing the surface defects. The incorporation of Mg into ZnO is expected to reduce the formation of oxygen vacancies owing to the strong interaction between Mg^{2+} and O^{2-} ions. However, the study of $Mg_xZn_{1-x}O$ based Schottky diode is very limited. S. K. Mohanta et al. [51] studied the Pt Schottky diode based on H_2O_2 treated MgZnO:N films and resulted in a relatively good Schottky properties with the ideality factor (n) of 2.79 and Schottky barrier height (Φ_B) of 0.69 eV. Wang et al. [52] discussed a Schottky type metal−semiconductor-metal photodetector. The interdigital Au fingers were used as the contact electrode. The contact Au/MgZnO shows rectified characteristics and the dark current of the photodetector is about 6.5 pA at a bias voltage of 10 V. To expand the application of $Mg_xZn_{1-x}O$ film in deep-ultraviolet optoelectronic devices, both high quality $Mg_xZn_{1-x}O$ film and good electricity of metal/$Mg_xZn_{1-x}O$ Schottky contact are needed.

In this work, we present the Schottky contact properties of Ag metal on $Mg_xZn_{1-x}O$ ($0 \leq x \leq 0.18$) thin films as the function of Mg content without surface treatment. The $Mg_xZn_{1-x}O$ films were deposited by RF magnetron co-sputtering with ZnO and $Mg_{0.3}Zn_{0.7}O$ targets. The Mg content was controlled by varying the RF power of $Mg_{0.3}Zn_{0.7}O$ target, while the power applied at ZnO target was remained at 100W. The structural properties of these films are also reported.

4.2.1.2 Experimental detail

The ternary $Mg_xZn_{1-x}O$ thin films were deposited on n-Si (100) substrates by RF co-sputtering. Silicon substrates yield a resistivity of 0.5-8 $\Omega\cdot$cm in conjunction with an n-type carrier. The co-sputtered commercial targets, ZnO and $Mg_{0.3}Zn_{0.7}O$ (4 inch in diameter, Mg/(Mg+Zn), 30 at.%), had purity of 99.99 %. Before loading into the sputtering chamber, the Si substrates were cleaned with acetone, methanol, and de-ionized water in an ultrasonicator for 15 min. The base pressure was less than 10^{-6} Torr, and the working pressure was 5 mTorr. Argon gas was introduced at a flow rate of 20 cm^3/min, which was controlled by using a mass flow controller. The ZnO and $Mg_xZn_{1-x}O$ films were deposited for 90 min at 300 ℃. The RF power of ZnO target was 100 W, which was remained unchanged, whereas the power applied at $Mg_{0.3}Zn_{0.7}O$ target was set to 0W, 50 W, 100 W, and 150 W, the corresponding samples are designated as ZnO, MZO50, MZO100, and MZO150, respectively.

After deposition, a lateral Schottky diode in Figure 4.8 was fabricated by photolithography. The fabrication process is described as Figure 4.9. The annular Ti (10 nm)/Au(50 nm) ohmic rings in Figure 4.8 (a) deposited by electron beam (e-beam) evaporation was formed by lift-off photolithography. To form ohmic contacts the Ti/Au contact metals were post-annealed at 300 ℃ in vacuum for 3 min by rapid thermal process. Then the inner circle of Ag (50 nm) Schottky contact was fabricated by lift-off photolithography and e-beam evaporation. Figure 4.8 (b) shows the schematic cross section of the fabricated devices.

The Mg concentration was confirmed by energy dispersive X-ray spectrum (EDS, Tescan, MIRA-3). The structure characteristics were investigated by the X-ray diffraction (XRD, Rigaku, Smartlab) spectrum. The surface morphologies were characterized by the atomic force microscopy (AFM, Park systems, XE-100). The *I-V* characteristics were evaluated by the semiconductor parameter analysis (Hewlett-Packard, HP-4145B). The electrical properties were measured by Hall effect measurement (Ecopia, HMS-5000).
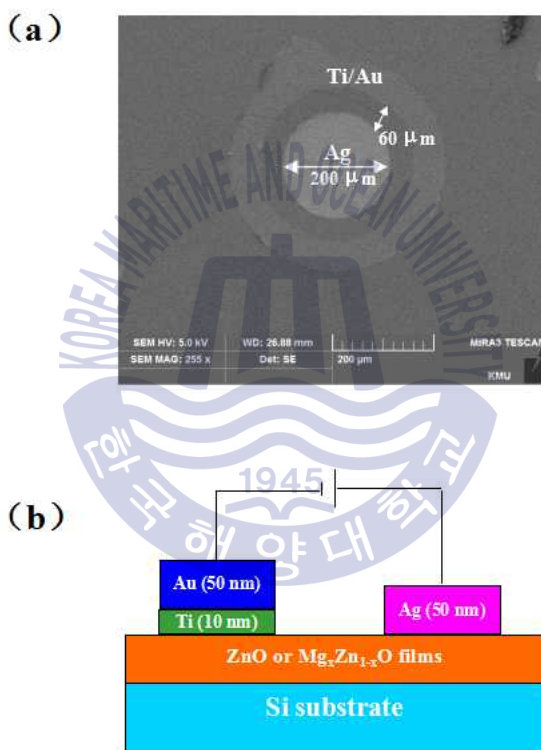

Fig. 4.8 (a) SEM image showing a top view of the lateral Schottky diode pattern and (b) a schematic cross section of the Schottky diode
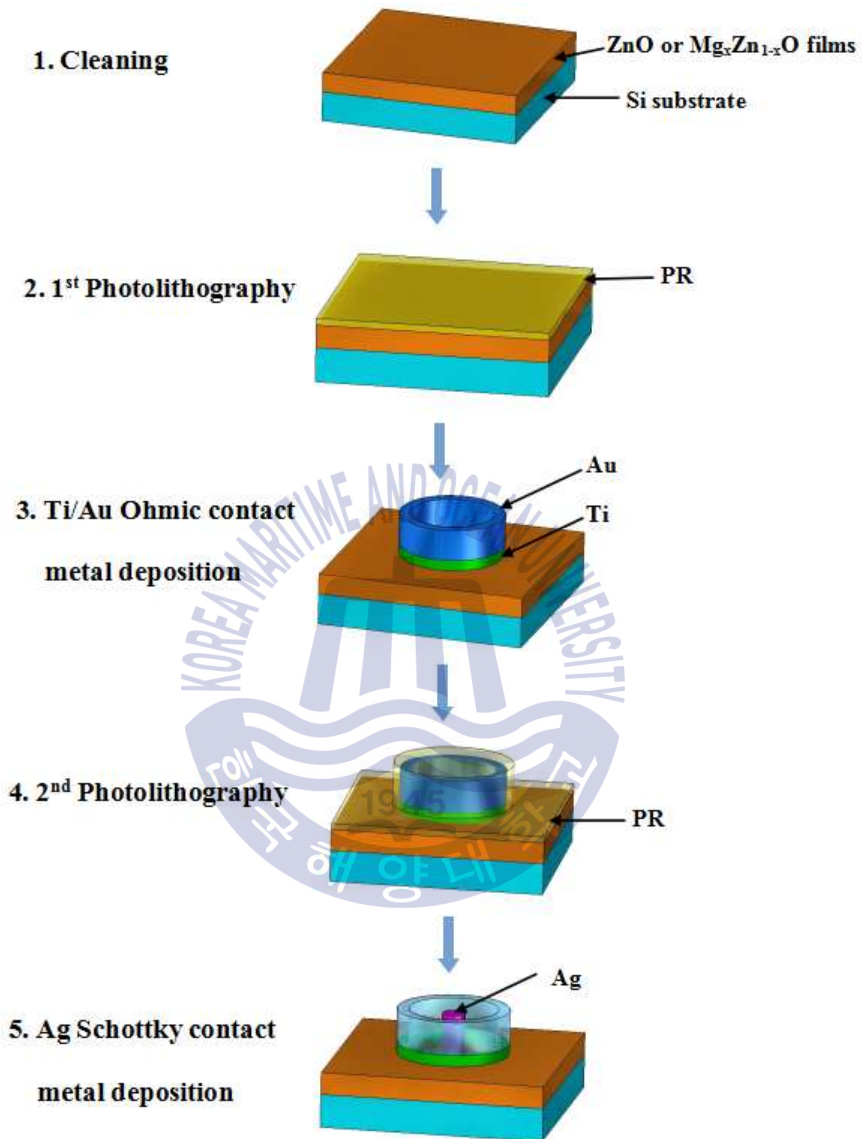
Fig. 4.9 The charts of the fabrication process of lateral Schottky diode

Collection

4.2.1.3 Results and discussions

The Mg concentration of $Mg_xZn_{1-x}O$ film was confirmed by EDS measurement. Mg compositions, the ratio of Mg/(Mg+Zn) at.%, in MZO50, MZO100, and MZO150 are 2 at.%, 11 at.%, and 18 at.%, respectively. The Mg content increases as the power of $Mg_{0.3}Zn_{0.7}O$ target increases. With the increasing in RF power of $Mg_{0.3}Zn_{0.7}O$ target, more plasma particles strike the $Mg_{0.3}Zn_{0.7}O$ target and eject more MgZnO atoms to the Si substrate. So the Mg content of $Mg_xZn_{1-x}O$ film increases as the RF power of $Mg_{0.3}Zn_{0.7}O$ target increases. Figure 4.10 (a) shows the XRD diffraction patterns of ZnO, MZO50, MZO100, and MZO150 thin films. All samples predominantly show the (002) direction with hexagonal wurtzite structure. The ZnO (002) diffraction peak is 34.3° whereas the MZO50, MZO100, and MZO150 thin films display hexagonal MgZnO (002) peak at 34.3°, 34.34°, and 34.38°, which shifts to the 34.44° observed for single $Mg_{0.3}Zn_{0.7}O$ target. This indicates an increase in the incorporation of Mg into ZnO, which is consistent with the EDS result. The full widths at half maxima (FWHM) of $Mg_xZn_{1-x}O$ thin films increases from 0.37° to 0.7° as the Mg concentration increases from 2 at.% to 18 at.% as shown in Figure 4.10 (b). This is because that the incorporation of Mg into ZnO results in lattice distortion owing to the difference between Zn^{2+} (0.60 Å) and Mg^{2+} (0.57 Å) ionic radius.

Figure 4.11 shows the AFM results of $Mg_xZn_{1-x}O$ thin films. The surfaces of the $Mg_xZn_{1-x}O$ thin films reveal grain-shaped islands. The value of the root-mean-square (RMS) roughness is from 5.6 nm to 7.5 nm. The grain sizes of ZnO, MZO50, MZO100, and MZO150 are 61.7 nm, 73.2 nm, 80.5 nm, and 90.5 nm, respectively.
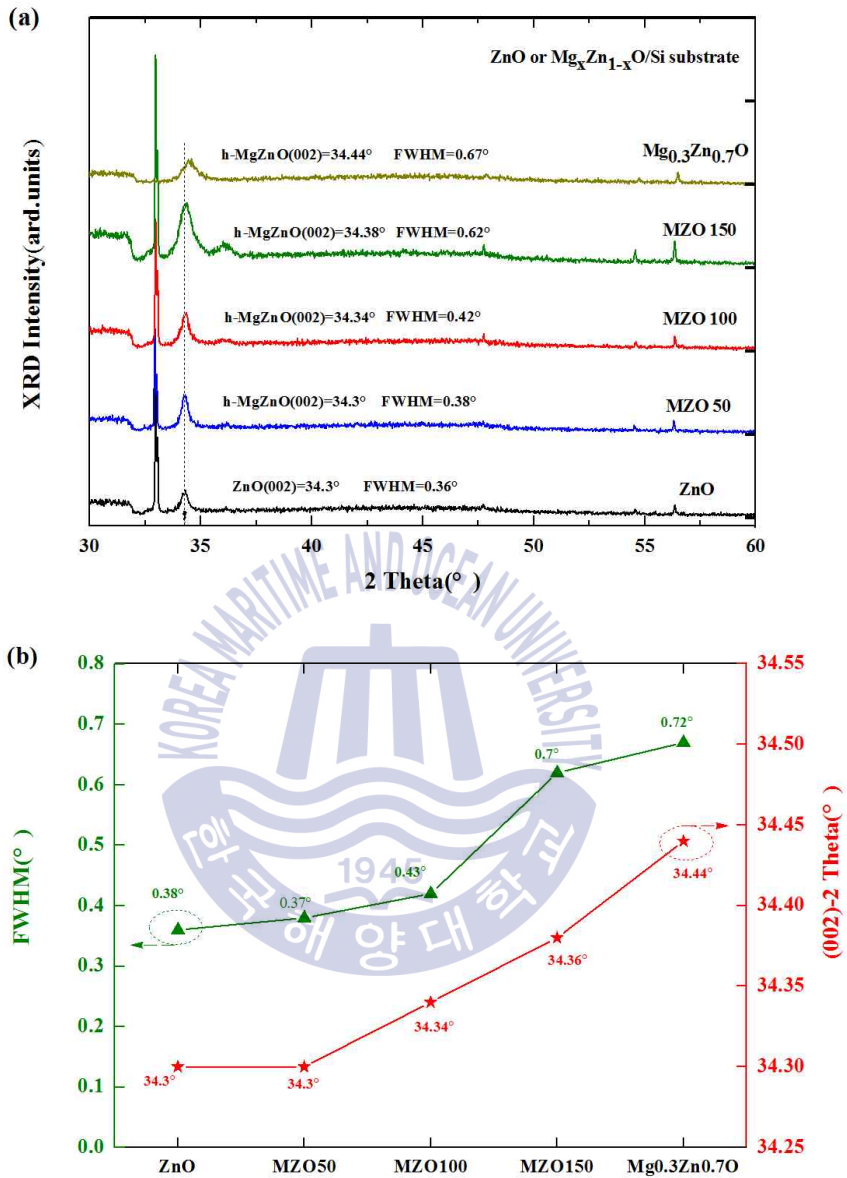
**Fig. 4.10** (a) XRD θ-2θ patterns for ZnO, MZO50, MZO100, MZO150, and Mg$_{0.3}$Zn$_{0.7}$O thin films as deposited, and (b) XRD results versus the Mg$_x$Zn$_{1-x}$O thin films with different Mg oncentration
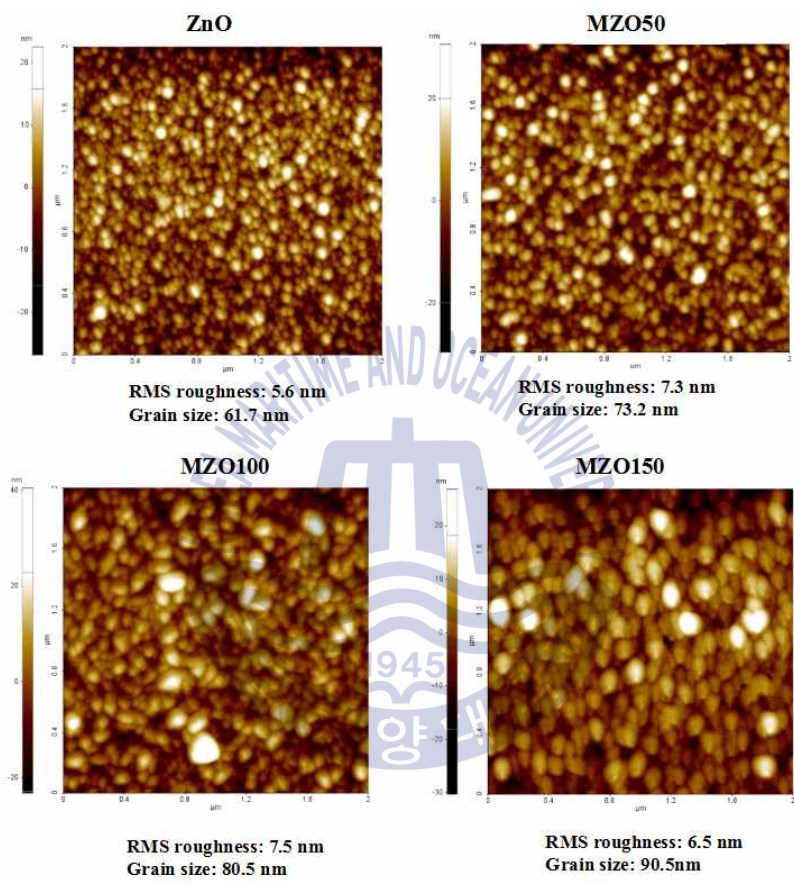
Fig. 4.11 Surface morphologies ($2 \times 2 ~\mu m^2$) of ZnO and $Mg_xZn_{1-x}O$ thin films as deposited

Figure 4.12 shows the *I-V* (black square-dotted line) which was measured at room temperature in dark, log|*I*|-*V* (red triangle-dotted line) of the Schottky diodes. The diode equation may be expressed as

$$I = I_0 \left[\exp\left(\frac{q(V - IR_S)}{nkT} \right) - 1 \right] \tag{4.4}$$

where I_0 is the saturation current, q is the electron charge, n is the ideality factor, k is the Boltzmann constant, R_s is the series resistance, and T is the absolute temperature.

Figure 4.12 (a) shows the *I-V* curve of the Ag Schottky diode fabricated on ZnO thin film. As the voltage increases, the currents increases linearly. The ZnO thin films displays a high carrier concentration of 7.95×10^{18} cm^{-3} (mobility: 33.9 cm^2/Vs, resistivity: 2.3×10^{-2} $\Omega \cdot$cm), measured by Hall effect measurement at room temperature. The metal contact on a high-carrier-density material forms an ohmic contact that exhibits a dominant tunneling current transport process. Figure 4.12 (b), (c), (d) show the *I-V* and log|*I*|-*V* curve of the Ag Schottky diode fabricated on MZO50, MZO100, and MZO150 thin films. The inserted figure shows the *I-V* characteristics between Ti-Au contacts on Mg$_x$Zn$_{1-x}$O thin films, which verifies the good ohmic contact properties. These devices showed a clear rectification behavior, with turn-on voltages of 0.31 V (MZO50), 0.32 V (MZO100), and 0.5 V (MZO150). The leakage currents of the Schottky diodes at a voltage of -1V were 3.21×10^{-4} A (MZO50), 1.22×10^{-5} A (MZO100), and 5.11×10^{-9} A (MZO150) at room temperature. The forward current (I_F)/reverse current (I_R) ratios of the Schottky diodes at ±1V were 2.10 (MZO50), 2.04 (MZO100), and 2.25×10^3 (MZO150). The Ag/MZO150 Schottky diode shows the highest rectifying ratios.
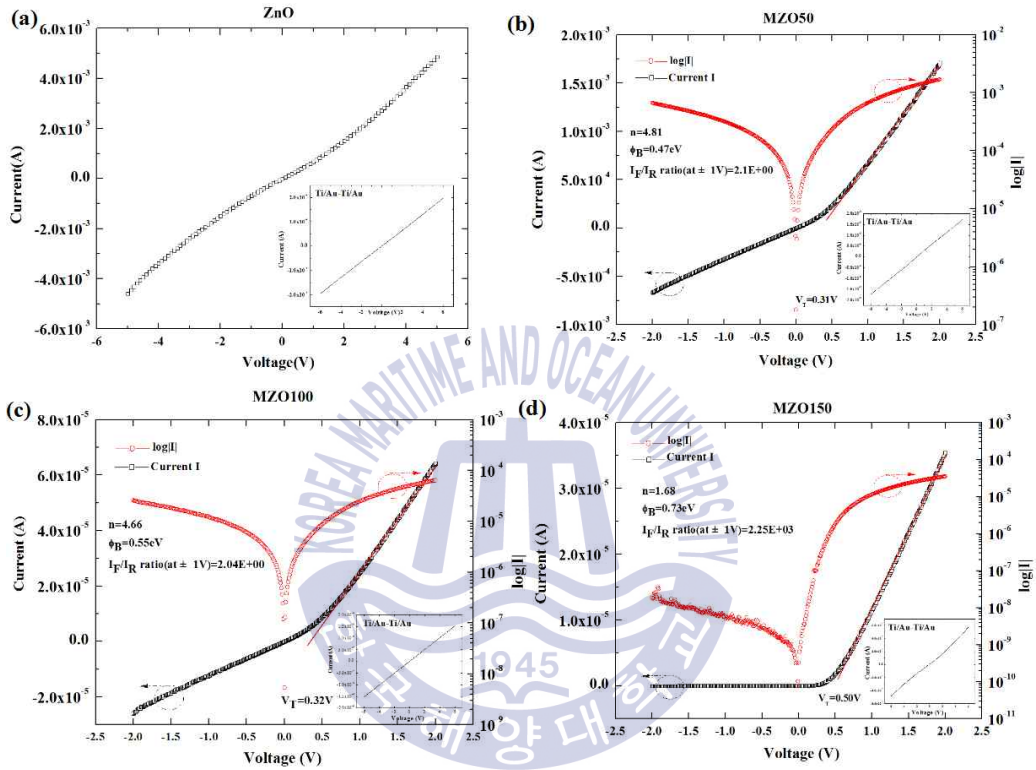
Fig. 4.12 *I-V* characteristics of Ag SCs on ZnO, MZO50, MZO100, and MZO150 thin films. The inserted figure shows the *I-V* characteristics between Ti/Au contacts on the ZnO and $Mg_xZn_{1-x}O$ thin films

The diode ideality factor (n) can be determined from the slope of semi-logarithmic forward bias $I–V$ plot for 0.25 > V > 3 kT/q according to Eq. 2.7. The ideality factor of MZO50, MZO100, and MZO150 are 4.81, 4.66, and 1.68, respectively. The n $\geqq$ 2 indicates that thermionic emission is no longer the dominant transport mechanism. In other words this behavior is often attributed to defect states in the band gap of the semiconductor providing other current transport mechanisms such as barrier tunneling or generation recombination in the space charge region [53]. High ideality factors have also been attributed to laterally inhomogeneous contacts caused by nonuniformities in the Schottky interface, such as structural defects, surface contamination, and variations in interface composition [53]. The Hall effect measurement results show that the carrier concentration of MZO50, MZO100, and MZO150 are 4.6×10^{18} cm^{-3}, 2.82×10^{18} cm^{-3}, and 1.59×10^{17} cm^{-3}, which decreases as the Mg concentration increases. This indicates that the incorporation of Mg into ZnO reduces the formation of oxygen vacancies which acting as donors for electrons below the contact. So the ideality factor decreases as the Mg concentration increases. The Ag/MZO150 Schottky diode displays the lowest n value of 1.68.

The Schottky barrier height was calculated as

$$I_0 = AA^* T^2 \exp\left(-\frac{q\Phi_B}{kT}\right) \tag{4.5}$$

where Φ_B is the barrier height, A is the area of the diode, and A* is the effective Richardson constant. I_0 is derived from the straight-line intercepts of the $\ln|I|$-V curves at V=0. If the effective Richardson constant for a material is known, Φ_B can be deduced from Eq. 2.6, however, the value of A* for MgZnO has not, to the best our knowledge, been reported. Thus, the value of Φ_B can be calculated only by using the estimated value of 32 Acm^{-2}K^{-2} for ZnO. The Φ_B values of MZO50, MZO100, and MZO150 are 0.47 eV, 0.55 eV, and 0.73 eV, which increases with the increasing in Mg concentration. Perkins et al. [54] reported that the incorporation of Mg into ZnO moved the conduction band minimum of ZnO up. That is, the electron affinity (χ_s) decreases as the Mg concentration increases.

According to the basic theory of Schottky contact formation $\Phi_B = \Phi_m - \chi_s$ developed by Schottky and Mott, the barrier height increases with the decreasing in electron affinity. What's more, with the increasing in Mg content, oxygen vacancies decreases and the effect of Fermi level pinning on Schottky barrier height is decreased. So the barrier height of Ag/Mg$_x$Zn$_{1-x}$O Schottky diode increases as the Mg concentration increases.

The IR$_s$ term in Eq. 4.4 is the voltage drop across series resistance of device. The values of the series resistance can be determined from the slope of a plot of $I/(\mathrm{d}I/\mathrm{d}V)$ versus I which would be linear under high voltage, as shown in Figure 4.13. This resistance was obtained by fitting the $I{-}V$ curves under the forward voltage exceeding 0.5 V where the log $|I|$-V curve began to deviate considerably from linearity due the effect of series resistance. As with p–n junction diode characteristics, the series resistance is affected by high applied voltages, which can be caused by excessive contact resistance. The series resistance of the Ag/MZO50, Ag/MZO100, and Ag/MZO150 Schottky diode are 9.43 $\times 10^2$ Ω, 2.25 $\times$ 10^4 Ω, and 3.74 $\times$ 10^4 Ω, respectively. The series resistance increases with the increasing in Mg content in Mg$_x$Zn$_{1-x}$O films. According to the previous research, the special contact resistivity of ohmic contact increases as the Mg content increases owing to the reduction of oxygen vacancies. What's more, the resistivity of Mg$_x$Zn$_{1-x}$O films increases as the Mg content increases. Because the incorporation of Mg into ZnO results in lattice distortion to some extent which increases the lattice scattering. The increased special contact resistivity and resistivity of Mg$_x$Zn$_{1-x}$O films are the main point why the series resistance of Schottky devices increases with the increasing in Mg concentration. This also explains why the turn on voltage increases with the increasing in Mg concentration. That is, more Mg ion in the thin film need more voltages to provide sufficient energy for electrons to jump over the barrier at the metal-semiconductor junction.
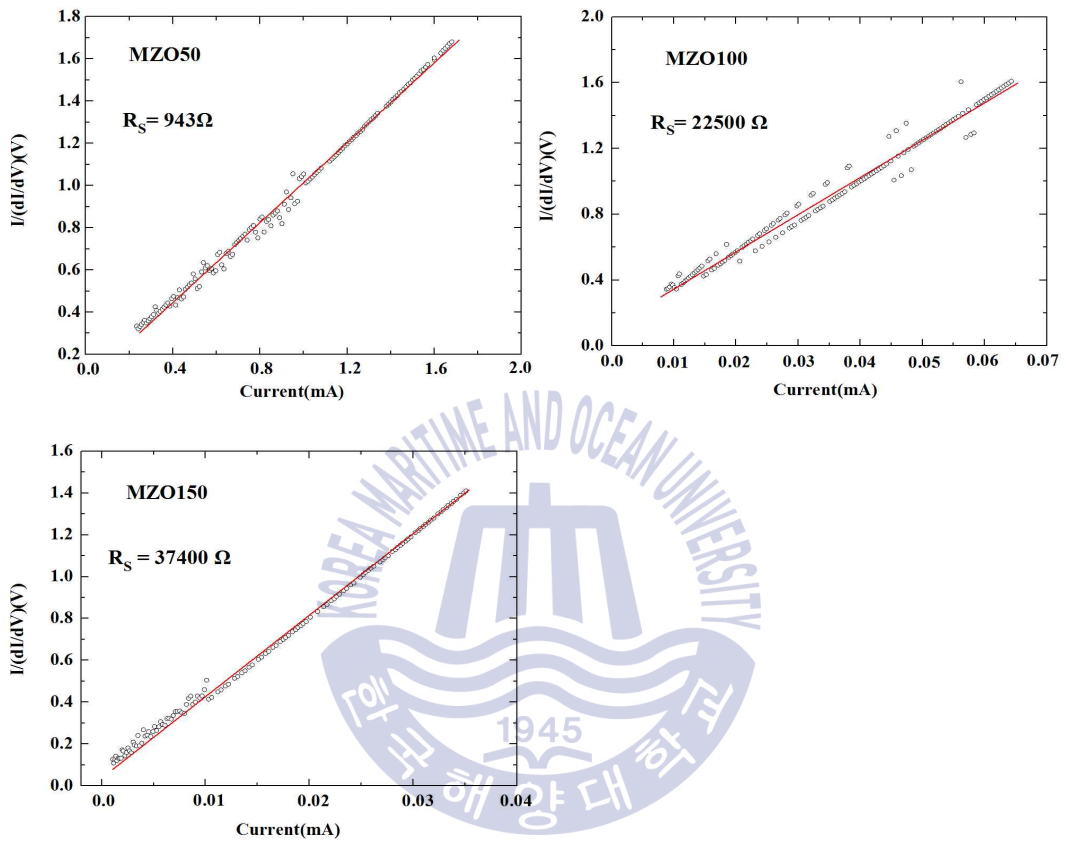
Fig. 4.13 *I/(dI/dV)* vs current for the Ag/MZO50, Ag/MZO100, and Ag/MZO150 Schottky diodes

The electrical properties of Ag SCs on ZnO, MZO50, MZO100, and MZO150 are summarized as Table 4.1. The Schottky contact properties are improved as the Mg content is increased owing to the reduction of oxygen vacancies. The Ag Schottky diode based on MZO150 (Mg: 18 at.%) shows the best electrical characteristics with the effective barrier height of 0.73 eV, the ideality factor of 1.68, and the high I_F/I_R ratios of 2.25×10^3 at $\pm 1V$.

Table 4.1 Electrical properties of Schottky diodes based on ZnO, MZO50, MZO100, and MZO150 thin film with Ag metal

Ag SCs	Is (A)	VT (V)	n	Φ_B (ev)	$(I_F)/(I_R)$ ratio	R_S (Ω)
ZnO	--	--	--	--	--	--
MZO50 (Mg:2at.%)	1.54×10^{-5}	0.31	4.81	0.47	2.10×10^0	9.43×10^2
MZO100 (Mg:11at.%)	6.16×10^{-7}	0.32	4.66	0.55	2.04×10^0	2.25×10^4
MZO150 (Mg:18at.%)	5.91×10^{-10}	0.5	1.68	0.73	2.25×10^3	3.74×10^4

4.2.1.4 Conclusions

The Ag Schottky diodes based on $Mg_xZn_{1-x}O$ thin films with the Mg content ranging from 0 to 18 at.% are presented in the research. MZO50, MZO100, and MZO150 based Schottky diodes showed rectifying I-V characteristics while ZnO based diode exhibited linear I-V characteristics. The Schottky properties were improved by the incorporation of Mg into ZnO. The barrier height increased and the ideality factor decreased as the Mg content increased. The device based on MZO150 (Mg: 18 at.%) displayed superior electrical characteristic with the barrier height of 0.73 eV, the ideality factor of 1.68, and the high I_F/I_R ratios of 2.25 $\times$ 10^3 at ± 1V.

4.2.2 Schottky diodes prepared with Ag, Au, and Pd contacts on $Mg_{0.18}Zn_{0.82}O$ film

4.2.2.1 Experiment details

The ternary $Mg_{0.18}Zn_{0.82}O$ thin film was deposited on n-Si (100) substrates by RF co-sputtering. Silicon substrates yield a resistivity of 0.5-8 $\Omega \cdot cm$ in conjunction with an n-type carrier. The co-sputtered commercial targets, ZnO and $Mg_{0.3}Zn_{0.7}O$ (4 inch in diameter, Mg/(Mg+Zn), 30 at.%), had purity of 99.99 %. Before loading into the sputtering chamber, the Si substrates were cleaned with acetone, methanol, and de-ionized water in an ultrasonicator for 15 min. The base pressure was less than 10^{-6} Torr, and the working pressure was 5 mTorr. Argon gas was introduced at a flow rate of 20 cm^3/min, which was controlled by using a mass flow controller. The RF power of ZnO target was 100 W and the power applied at $Mg_{0.3}Zn_{0.7}O$ target was set to 150 W. The ZnO and $Mg_xZn_{1-x}O$ films were deposited for 90 min at 300 ℃. After deposition, a lateral Schottky diode was fabricated by photolithography. The annular Ti (10 nm)/Au(50 nm) ohmic rings deposited by electron beam (e-beam) evaporation was formed by lift-off photolithography. To form ohmic contacts the Ti/Au contact metals were post-annealed at 300 ℃ in vacuum for 3 min by rapid thermal process. Then the inner circle Ag, Au and Pd (50 nm) Schottky contact were fabricated by lift-off photolithography and e-beam evaporation.

The Mg concentration was confirmed by energy dispersive X-ray spectrum (EDS, Tescan, MIRA-3). The structure characteristics were investigated by the X-ray diffraction (XRD, Rigaku, Smartlab) spectrum. The surface morphologies were characterized by the atomic force microscopy (AFM, Park systems, XE-100). The *I-V* characteristics were evaluated by the semiconductor parameter analysis (Hewlett-Packard, HP-4145B). The electrical properties were measured by Hall effect measurement (Ecopia, HMS-5000).

4.2.2.2 Results and discussions

The Mg composition of $Mg_xZn_{1-x}O$ was identified as 18 at.% by EDS measurement. Figure 4.14 (a) shows the XRD diffraction pattern of $Mg_{0.18}Zn_{0.82}O$ thin film. The $Mg_{0.18}Zn_{0.82}O$ thin film predominantly shows the (002) direction with hexagonal wurtzite structure. In addition, by substituting of Mg^{2+} ions for Zn^{2+} ions, the lattice constant of c-axis direction is decreased due to the strong interaction between Mg^{2+} ions and O^{2-} ions. This phenomenon is confirmed that the $Mg_{0.18}Zn_{0.82}O$ (002) diffraction peak is 34.38 °, which is larger than ZnO (002) of 34.3 °.

Figure 4.14 (b) shows the surface image of $Mg_{0.18}Zn_{0.82}O$ thin film by using an atomic microscopy. The root-mean-square roughness is 6.5 nm and the grain-size is 90.5 nm.
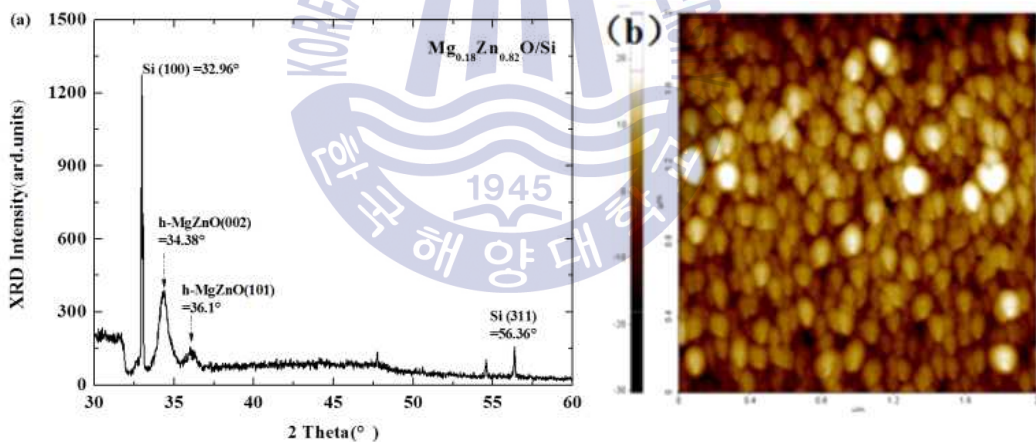

Fig. 4.14 (a) XRD and (b) AFM surface morphology of the $Mg_{0.18}Zn_{0.82}O$ film

Figure 4.15 shows the *I-V* (black square-dotted line) which was measured at room temperature in dark, log|*I*|-*V* (red triangle-dotted line) of the Schottky diodes. The diode equation may be expressed as

$$I = I_0 \left[\exp\left(\frac{q(V - IR_S)}{nkT} \right) - 1 \right] \quad (4.6)$$

where

$$I_0 = AA^* T^2 \exp\left(-\frac{q\Phi_B}{kT} \right) \quad (4.7)$$

where I_0 is the saturation current, q is the electron charge, n is the ideality factor, k is the Boltzmann constant, R_s is the series resistance, and T is the absolute temperature. In the formulation of saturation current I_0, Φ_B is the barrier height, A is the area of the diode, and A* is the effective Richardson constant. The diode ideality factors for the cases of Ag, Au, and Pd are 1.68, 3.30, and 4.54, respectively. The value of n is determined at a low forward bias for 0.25 > V > 3 kT/q, and the *I-V* curves show an exponential linear increase in this region. Ag has the smallest n value of 1.68, but Au and Pd show relatively high ideality factors. This is because that metal Au and Pd can form eutectics with Zn and form interface layers with not only electric dipoles but also native defects that can act as electrically active donors or acceptors, hopping sites, as well as recombination centers [26].

From Figure 4.15, these devices show a clear rectification behavior, with turn-on voltages of 0.50 V (Ag), 0.24 V (Au), and 0.15 V (Pd). The leakage currents of the Schottky diodes at a voltage of -1V are 5.11×10^{-9} A (Ag), 1.12×10^{-6} A (Au), and 2.60×10^{-6} A (Pd) at room temperature. The forward current (I_F) /reverse current (I_R) ratios of the Schottky diodes at ±1V are 2.25×10^3 (Ag), 8.21 (Au), and 7.08 (Pd). The $Ag/Mg_{0.18}Zn_{0.82}O$ Schottky diode shows the highest rectifying ratios. The superior rectification properties of the Schottky diode should be have the low leakage current under a reverse bias and the low series resistance under a forward bias.
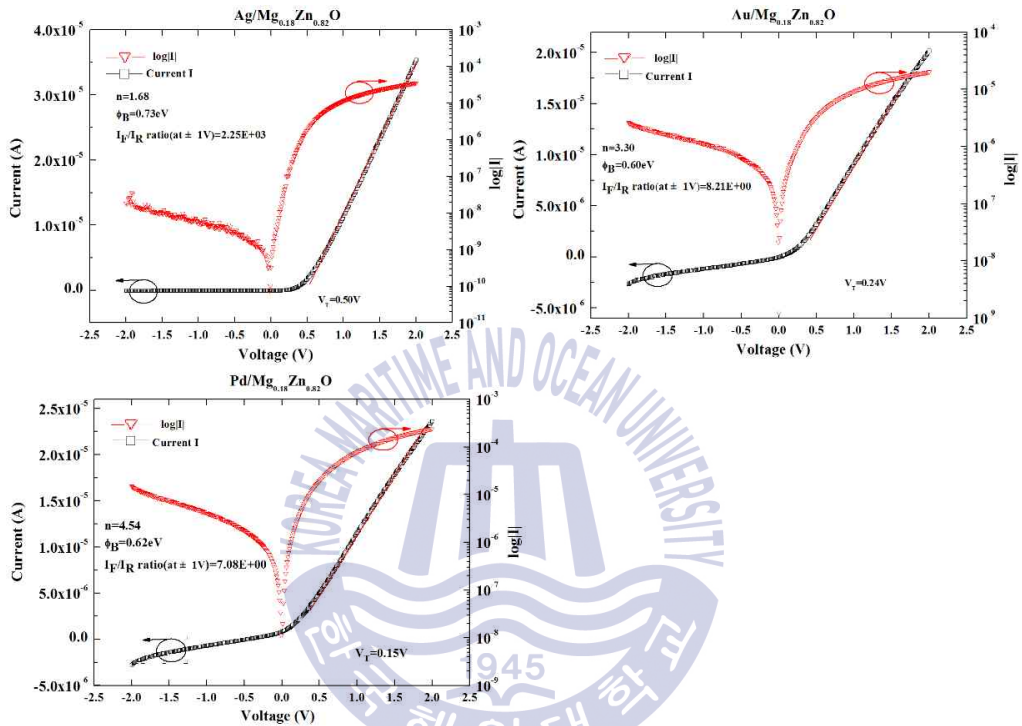
Fig. 4.15 *I-V* characteristics of Ag, Au, and Pd SCs based on Mg$_{0.18}$Zn$_{0.82}$O thin films

The slope of a plot of $I/(dI/dV)$ versus I yields the series resistance (R_s), as shown in Figure 4.16. This resistance is obtained by fitting the $I-V$ curves under the forward voltage exceeding 0.5 V where the $\log|I|$-V curve begin to deviate considerably from linearity due the effect of series resistance. As with p–n junction diode characteristics, the series resistance is affected by high applied voltages, which can be caused by excessive contact resistance. The series resistance of Ag/$Mg_{0.18}Zn_{0.82}O$, Au/$Mg_{0.18}Zn_{0.82}O$, and Pd/$Mg_{0.18}Zn_{0.82}O$ Schottky diode are 3.74×10^4 Ω, 1.0×10^5 Ω, and 7.08×10^5 Ω, respectively. Au and Pd show relatively higher series resistances. This may result from the poor adhesion properties on $Mg_{0.18}Zn_{0.82}O$ surface that reduces the carrier injection characteristics and induces carrier trapping at the metal and semiconductor interface.

The Schottky barrier height is calculated as Eq. 4.7 by using the estimated value of $A^* = 32$ $Acm^{-2}K^{-2}$ for ZnO. I_0 is derived from the straight-line intercepts of the $\ln|I|$-V curves at V=0. The Φ_B values of Ag/$Mg_{0.18}Zn_{0.82}O$, Au/$Mg_{0.18}Zn_{0.82}O$, and Pd/$Mg_{0.18}Zn_{0.82}O$ are 0.73 eV, 0.60 eV, and 0.62 eV. The electrical properties of Schottky diode based on $Mg_{0.18}Zn_{0.82}O$ thin film with Ag, Au, and Pd Schottky electrodes are summarized as Table 4.2. Ag/$Mg_{0.18}Zn_{0.82}O$ Schottky diode exhibits the best properties with the barrier height of 0.73 eV, the ideality factor of 1.68, and the high I_F/I_R ratios of 2.25×10^3 at $\pm 1V$.

M.Salina et al. [55]. fabricated the Pd contacts on $Mg_xZn_{1-x}O$ ($0 \leq x \leq 0.3$) which was prepared by the sol-gel method and resulted non-rectification properties. Au was used as ohmic contact in Ag/$Mg_{0.1}Zn_{0.9}O$ Schottky diode fabricated by Huang et al. [56]. S. Han et al. [57] prepared the Au contact on as deposited $Mg_{0.27}Zn_{0.73}O$ film, but showed non-rectification behavior. However, in our case, both the Pd and Au contacts on $Mg_{0.18}Zn_{0.82}O$ films show good Schottky properties, which indicate the $Mg_xZn_{1-x}O$ films display relatively high quality with less native defects. Owing to the complicated surface quality of ZnO or $Mg_xZn_{1-x}O$ films, the Schottky barrier height between metal and ZnO or $Mg_xZn_{1-x}O$ is independent on the work function of metal. Up to now, the best ZnO based Schottky diode was

fabricated with Ag metal by M. W. Allen et al. [58]. Moreover, the Ag Schottky diode based on MgZnO/ZnO heterojunction was fabricated by J. H. Lee [59] with the barrier height of 0.73 eV and the ideality factor of 2.37. So the $Mg_{0.18}Zn_{0.82}O$ film based Schottky diode with Ag metal is promising for future application in UV optoelectronic devices.

Table 4.2 Electrical properties of Schottky diodes based on $Mg_{0.18}Zn_{0.82}O$ thin film with Ag, Au, and Pd metals

|	Is (A)	VT (V)	n	Φ_B (ev)	$(I_F)/(I_R)$ ratio	R_S (Ω)
Ag	5.91×10^{-10}	0.5	1.68	0.73	2.25×10^3	3.74×10^4
Au	8.34×10^{-8}	0.24	3.30	0.60	8.21	1.0×10^5
Pd	3.39×10^{-8}	0.15	4.54	0.62	7.08	5.08×10^5
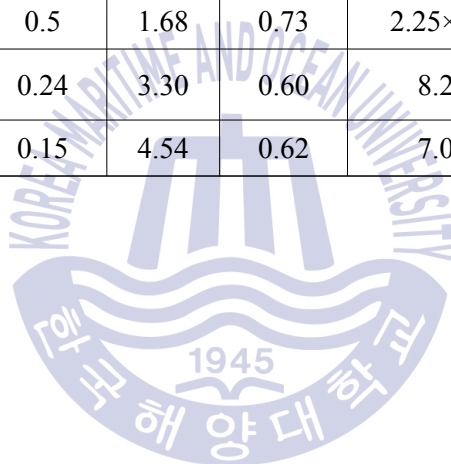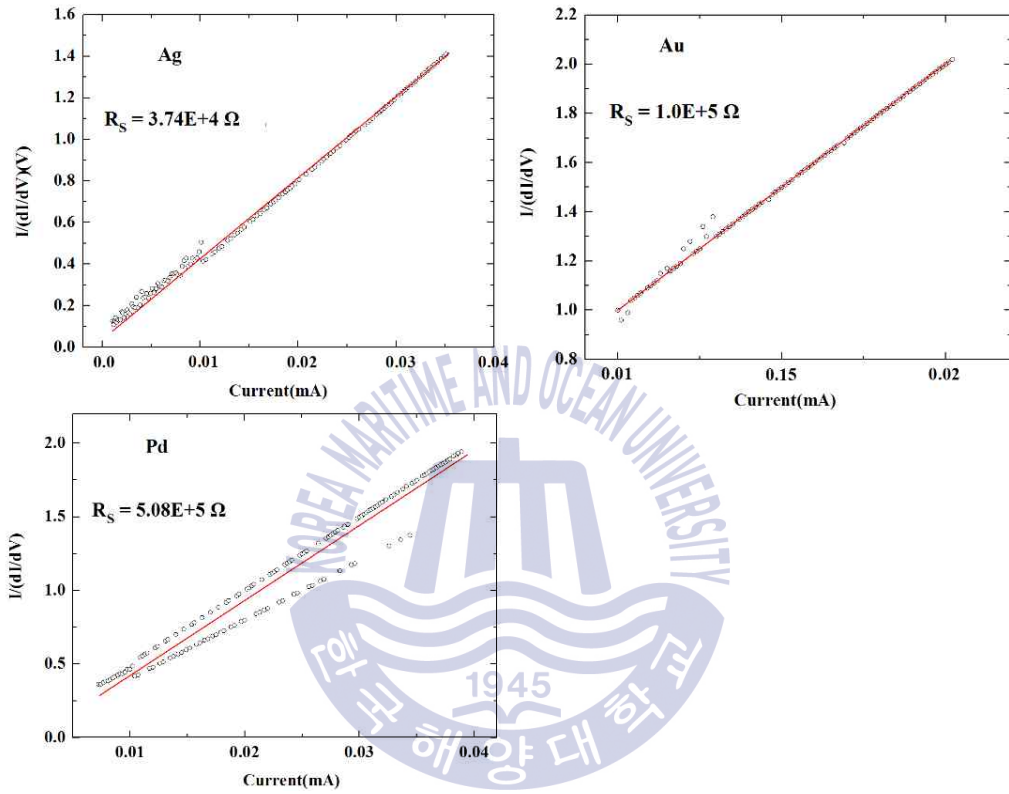
Fig. 4.16 *I/(dI/dV)* vs current for the Schottky diodes based on $Mg_{0.18}Zn_{0.82}O$ thin film with Ag, Au, and Pd metals

4.2.2.3 Conclusions

The Ag, Au, and Pd Schottky diodes based on $Mg_{0.18}Zn_{0.82}O$ thin films are presented in this research. All of these Schottky diodes showed rectifying *I-V* characteristics and good Schottky properties. What's more, the Ag Schottky diode displays superior electrical characteristic with the barrier height of 0.73 eV, the ideality factor of 1.68, and the high I_F/I_R ratios of 2.25×10^3 at $\pm 1V$. The $Mg_{0.18}Zn_{0.82}O$ film based Schottky diode with Ag metal is promising for future application in UV optoelectronic devices.

Chapter 5. Summary & Conclusion

This dissertation investigates the structural and electrical properties of $Mg_xZn_{1-x}O$ ($0 \leq x \leq 0.18$) thin films which were deposited by RF magnetron co-sputtering with ZnO and $Mg_{0.3}Zn_{0.7}O$ targets on Si substrate. The Mg content was varied by controlling the power of $Mg_{0.3}Zn_{0.7}O$ target. And then, the Schottky contact properties on $Mg_xZn_{1-x}O$ thin films were explored.

The $Mg_xZn_{1-x}O$ thin films annealed at 750 ℃ for 60 min, with Mg content from 0 at.% to 18 at.%, showed hexagonal wurtzite structure with preferential c-axis orientation. The h-MgZnO (002) diffraction peak and the FWHM of $Mg_xZn_{1-x}O$ thin films increased as the Mg concentration increased. AFM analysis revealed that the surface images were similar as compare with ZnO and $Mg_xZn_{1-x}O$ thin films. On the other hand, the resistivity of $Mg_xZn_{1-x}O$ thin films increased with the Mg content increasing. The carrier concentration decreased from 1.17×10^{19} cm^{-3} to 1.17×10^{17} cm^{-3} as the Mg concentration increased from 0 at.% to 18 at.% indicating the decreases of oxygen vacancies. Meanwhile, the Hall mobility was increased.

The Schottky contact properties on $Mg_xZn_{1-x}O$ thin films as the function of Mg content were investigated by fabricating the lateral Schottky diode with Ag metal. MZO50, MZO100, and MZO150 based Schottky diodes showed rectifying I-V characteristics while ZnO based diode exhibited linear I-V characteristics. The Schottky properties were improved by the incorporation of Mg into ZnO. The barrier height increased and the ideality factor decreased as the Mg content increased owing to the reduction of oxygen vacancies. The device based on MZO150 (18 at.%) displayed superior electrical characteristic with the barrier height of 0.73 eV, the ideality factor of 1.68, and the high I_F/I_R ratios of 2.25×10^3 at ±1V, which is promising for future application in UV optoelectronic devices.

Finally, the Au and Pd Schottky diodes were fabricated on $Mg_{0.18}Zn_{0.82}O$ thin films and showed good Schottky properties.

Reference

[1] D. C. Look: Mater. Sci. Eng. B80 (2001) 383.

[2] D. C. Look, J. W. Hemsky, and J. R. Sizelove: Phys. Rev. Lett. 82 (1999) 2552.

[3] F. Tuomisto, K. Saarinen, D. C. Look, and G. C. Farlow: Phys. Rev. B72 (2005) 085206.

[4] H. Zheng, X. L. Du, Q. Luo, J. F. Jia, C.Z. Gu, and Q. K. Xue: Thin Solid Films 515 (2007) 3967.

[5] Leonard J. Brillson and Yicheng Lu: Journal of Applied Physics 109 (2011) 121301.

[6] L. K. Wang, Z. G. Ju, J. Y. Zhang, J. Zheng, D. Z. Shen, B. Yao, D. X. Zhao, Z. Z. Zhang, B. H. Li, and C. X. Shan: Appl. Phys. Lett. 95 (2009) 131113.

[7] X. Chen and J. Kang: Semiconductor Science and Technology 23 (2008) 025008.

[8] E.M. Levin, C.R. Robbins, H.F. McMurdie, M.K. Reser: Phase Diagrams for Ceramicists, American Ceramic Society, Columbus, Ohio, 1964.

[9] A. Ohtomo, M. Kawasaki, T. Koida, K. Masubuchi, H. Koinuma,Y. Sakurai, Y. Yoshida, T. Yasuda and Y. Segawa: Appl. Phys. Lett. 72 (1988) 2466.

[10] J.P. Kar, M.C. Jeong, W.K. Lee, J.M. Myoung: Materials Science and Engineering B 147 (2008) 74.

[11] Young Yi Kim, Bo Hyun Kong, Mi Kyung Choi, Hyung Koun Cho: Materials Science and Engineering B 165 (2009) 80.

[12] Si Woo Kang, Young Yi Kim, Cheol Hyoun Ahn, Sanjay Kumar Mohanta, and Hyung Koun Cho, J Mater Sci: Mater Electron 19, 755 (2008).

[13] Ü. Özgür, Ya. I. Alivov, C. Liu, A. Teke, M. A. Reshchikov, S. Doğan, V. Avrutin, S.-J. Cho, and H. Morkoçd: Journal of Applied Physics 98 (2005) 041301.

[14] T. Hanada: Advances in Materials Research 12 (2009) 1.

[15] Y. Liu, Q.Y. Hou, H.P. Xu, L.M. Li, Y. Zhang: Physica B 407 (2012) 2359.

[16] D. K. Hwang, M. C. Jeong, J. M. Myoung: Appl. Surf. Sci. 225 (2004) 217.

[17] S. J. Pearton, D. P. Norton, K. Ip, Y. W. Heo and T. Steiner: Journal of Vacuum Science & Technology B: Microelectronics and Nanometer Structures 22 (2004) 932.

[18] H. Kupfer, R. Kleinhempel, F. Richter, C. Peters, U. Krause, T. Kopte, and Y. Cheng, Journal of Vacuum Science & Technology A: Vacuum, Surfaces, and Films 24 (2006) 106.

[19] V. V. Afanas'ev, A. Stesmans, K. Cherkaoui, and P. K. Hurley, Appl. Phys. Lett. 96 (2010) 052103.

[20] I. Takeuchi, W. Yang, K.S. Chang, M.A. Aronova, T. Venkatesan, J. Appl. Phys. 94 (2003) 7334.

[21] L.K. Wanga, Z.G.Ju, C.X.Shan, J.Zheng, B.H.Li, Z.Z.Zhang, B.Yao, D.X.Zhao, D.Z. Shen and J.Y.Zhang: Journal of Crystal Growth 312 (2010) 875.

[22] Vilmantas Šukauskas: Characterization of MgZnO epitaxial layers with high Mg concentration, p5

[23] C. W. Teng, J. F. Muth, U. Ozgur, M. J. Bergmann, H. O. Everitt, A. K. Sharma, C. Jin and J. Narayan: Appl. Phys. Lett. 76 (2000) 979.

[24] Y. W. Heo, Y. W. Kwon, Y. Li, S. J. Pearton and D. P. Norton: Appl. Phys. Lett. 84 (2004) 3474.

[25] Ü. Özgür, Y. I. Alivov, C. Liu, A. Teke, M.A. Reshchikov, S. Doğan, V. Avrutin, S.-J. Cho, H. Morkoç: J. Appl. Phys. 98 (2005) 041301.

[26] L.J. Brillson, Y. Lu: J. Appl. Phys. 109 (2011) 121301.

[27] K. Liu, M. Sakurai, M. Aono: Sensors 10 (2010) 8604.

[28] E.S. Ates, S. Kucukyildiz, H.E. Unalan: Appl. Mater. Interf. 4 (2012) 5142.

[29] Pei-NanNi, C.X. Shan, S.P. Wang, B.H. Li, Z.Z. Zhang, D.X. Zhao, L. Liu, D.Z. Shen: J. Phys. Chem. C 116 (2012) 1350.

[30] D. C. Look, D. C. Reynolds, J. W. Hemsky, R. L. Jones, J. R. Sizelove: Appl. Phys. Lett. 75 (1999) 811.

[31] Chennupati Jagadish, Stephen Pearton: Zinc Oxide Bulk, Thin Films and Nanostructures: (Australia, 2006) 1rd ed., pp. 17.

[32] Robert F. Pierret: Semiconductor Device Fundamentals, (America, 1996）pp. 447~497.

[33] S. M, SZE: Semiconductor Devices, Physics and Technology, (USA, 2002) 2rd ed., pp. 225.

[34] E.H. Rhoderick, R.H. Williams: Metal‐semiconductor Contacts, 2nd ed., Clarendon, Oxford, 1988.

[35] C. Sah, R. N. Noyce, and W. Shockley: Proc. IRE 45 (1957) 1228.

[36] W. Liu, Electron: Lett, 28 (1992) 379.

[37] J. N. Shah, Y. L. Li, Th. Gessmann, and E. F. Schubert: J. Appl. Phys. 94 (2003) 2627.

[38] L. L. Chen, Z. Z. Ye, J. G. Lu, and P. K. Chu: Appl. Phys. Lett. 89 (2006) 252113.

[39] Ben G. Streetman and Sanjay Kumar Banerjee: Solid State Electronic Devices 6ed, (Austin, 2006) pp. 233.

[40] W. L. Guan, J. Lian, Y. X. Yu, Z. Z. Sun, M. L. Zhao, X. Wang, and W. F. Zhang: Optik 125 (2014) 5167.

[41] C. Y. Hu, Z. X. Qin, Z. X. Feng, Z. Z. Chen, Z. B. Ding, Z. J. Yang, T. J. Yu, X. D. Hu, S. D. Yao, G.Y. Zhang: Mater. Sci. Eng. B 128 (2006) 37.

[42] H. H. Berger: Solid-State Electron. 15 (1972) 145.

[43] Wen Chen, Jing Wang, and Min-rui Wang: Vacuum 81 (2007) 894.

[44] M. Lorenz, E. M. Kaidashev, H.von Wenckstern, V. Riede, C. Bundesmann, D. Spemann, G. Benndorf, H. Hochmuth, A. Rahm, H.-C. Semmelhack, and M. Grundmann: Solid-State Electron. 47 (2003) 2205.

[45] F. J. Klüpfel, H. von Wenckstern, and M. Grundmann: Appl. Phys. Lett. 106 (2015) 033502.

[46] L. J. Brillson, H. L. Mosbacker, M. J. Hetzer, Y. Strzhemechny, G. H. Jessen, D. C. Look, G. Cantwell, J. Zhang, and J. J. Song: Appl. Phys. Lett. 90 (2007) 102116.

[47] D. C. Oh, J. J. Kim, H. Makino, T. Hanada, M. W. Cho, T. Yao, and H. J.Ko: Appl. Phys. Lett. 86 (2005) 042110.

[48] S. Kim, H. Kim, and T. Seong: Appl. Phys. Lett. 86 (2005) 112101.

[49] B. J. Coppa and R. F. Davis: Appl. Phys. Lett. 82 (2003) 400.

[50] S.-H. Kim, H.-K. Kim, and T.-Y. Seong: Appl. Phys. Lett. 86 (2005) 112101.

[51] S.K. Mohanta, A. Nakamura, G. Tabares, A. Hierro, Á. Guzmán, E.Muñoz, and J. Temmyo: Thin Solid Films 548 (2013) 539.

[52] L.K. Wang, Z.G. Ju, C.X. Shan, J. Zheng, D.Z. Shen, B. Yao, D.X. Zhao, Z.Z. Zhang, B.H. Lia, J.Y. Zhang: Solid State Commun 149 (2009) 2021.

[53] M. W. Allen and S. M. Durbin: Appl. Phys. Lett. 92 (2009) 122110.

[54] J. Perkins, G. M. Foster, M. Myer, S. Mehra, J. M. Chauveau, A. Hierro, A. Redondo-Cubero, W. Windl, and L. J. Brillson: APL Material 3 (2015) 062801.

[55] M.Salina, M.Z.Sahdan, R.Ahmad, and M.Rusop: ICSE 2010 Proc. 2010, Melaka, Malaysia.

[56] Wen-Chang Huang, Tien-Chai Lin, Tsung-Lieh Hsien, Meng-Hua Tsai, Chia-Tsung Horng, Tsung-Lin Kuo: Microelectronic Engineering 107 (2013) 205.

[57] S. Han, J. Y. Zhang, Z. Z .Zhang, L. K. Wang, Y. M. Zhao, J. Zheng, J. M. Cao, B. Yao, D. X. Zhao, and D. Z. Shen: J. Phys. Chem. C 114 (2010) 21757.

[58] M. W. Allen, P. Miller, R. J. Reeves, and S. M. Durbin: Appl. Phys. Lett. 90, (2007) 062104.

[59] Jong Hoon Lee, Chang Hoi Kim, Ah Ra Kim, Hong Seung Kim, Nak Won Jang, Young Yun, Jin-Gyu Kim, Min Wook Pin, and Won Jae Lee: Jpn. J. Appl. Phys. 51, (2012) 0907.

Publication list

A. International Journal Publication (SCI, Co-author)

1. H. S. Kim, C. H. Kim, **L. L. Yue**, "A Study of the Growth of Single-Phase $Mg_{0.5}Zn_{0.5}O$ Films for UV LED", International Journal of Chemical, Molecular, Nuclear, Materials and Metallurgical Engineering **8**, 649 (2014).

B. Domestic Journal Publication

1. Y. B. Na, **L. L. Yue**, H. S. Kim, "A Study on Characteristics of a MgZnO Schottky Diode by Rapid Thermal Annealing of Ag Metal", Sae Mulli **8**, 725 (2015).

C. International Conference Presentations

1. **L. L. Yue**, H. S. Kim, N. W. Jang, "Electrical properties of $Mg_xZn_{1-x}O$ thin films deposited by RF co-sputtering", 7th International Symposium on Advanved Plasma Science and Its Applications for Nitrides and Nanomaterials, Nagoya Japan 26-31 March (2015).

2. **L. L. Yue**, J. H. Ock, H. S. Kim, N. W. Jang, "The Study of Ohmic Contact Properties to $Mg_xZn_{1-x}O$ alloy films deposited by RF co-sputtering", 14th International Union of Materials Research Societies-International Conference on Advanced Materials, Jeju Korea 25-29 October (2015).

3. J. H. Lee. **L. L. Yue**, H. S. Kim, N. W. Jang, W. J. Lee, "A study of thin film transistor using MgZnO/ZnO bilayer as active layer", 15th International Union of Materials Research Societies-International Conference on Advanced Materials, Fukuoka Japan 24-30 August (2014).

Acknowledgement